ISPRS Journal of Photogrammetry and Remote Sensing 123 (2017) 1–19

Contents lists available at ScienceDirect

ISPRS Journal of Photogrammetry and Remote Sensing

journal homepage: www.elsevier.com/locate/isprsjprs

Incorporation of satellite remote sensing pan-sharpened imagery into digital soil prediction and mapping models to characterize soil property variability in small agricultural fields

Yiming Xu [a,b,*], Scot E. Smith [a,b], Sabine Grunwald [a,c], Amr Abd-Elrahman [b,d], Suhas P. Wani [e]

[a] School of Natural Resource and Environment, University of Florida, 103 Black Hall, PO Box 116455, Gainesville, FL 32611, USA
[b] School of Forest Resources and Conservation – Geomatics Program, University of Florida, 301 Reed Lab, PO Box 110565, Gainesville, FL 32611-0565, USA
[c] Pedometrics, Landscape Analysis and GIS Laboratory, Soil and Water Science Department, University of Florida, 2181 McCarty Hall, PO Box 110290, Gainesville, FL 32611, USA
[d] Gulf Coast REC/School of Forest Resources and Conservation – Geomatics Program, University of Florida, 1200 N. Park Road, Plant City, FL 33563, USA
[e] International Crops Research Institute for the Semi-Arid Tropics (ICRISAT), Patancheru, 502324 Hyderabad, India

ARTICLE INFO

Article history:
Received 30 July 2016
Received in revised form 21 October 2016
Accepted 2 November 2016

Keywords:
Image pan-sharpening
Random forest
Digital soil mapping
Smallholder farm settings
Soil nutrients
South India

ABSTRACT

Soil prediction models based on spectral indices from some multispectral images are too coarse to characterize spatial pattern of soil properties in small and heterogeneous agricultural lands. Image pan-sharpening has seldom been utilized in Digital Soil Mapping research before. This research aimed to analyze the effects of pan-sharpened (PAN) remote sensing spectral indices on soil prediction models in smallholder farm settings. This research fused the panchromatic band and multispectral (MS) bands of WorldView-2, GeoEye-1, and Landsat 8 images in a village in Southern India by Brovey, Gram-Schmidt and Intensity-Hue-Saturation methods. Random Forest was utilized to develop soil total nitrogen (TN) and soil exchangeable potassium (K_{ex}) prediction models by incorporating multiple spectral indices from the PAN and MS images. Overall, our results showed that PAN remote sensing spectral indices have similar spectral characteristics with soil TN and K_{ex} as MS remote sensing spectral indices. There is no soil prediction model incorporating the specific type of pan-sharpened spectral indices always had the strongest prediction capability of soil TN and K_{ex}. The incorporation of pan-sharpened remote sensing spectral data not only increased the spatial resolution of the soil prediction maps, but also enhanced the prediction accuracy of soil prediction models.

Small farms with limited footprint, fragmented ownership and diverse crop cycle should benefit greatly from the pan-sharpened high spatial resolution imagery for soil property mapping. Our results show that multiple high and medium resolution images can be used to map soil properties suggesting the possibility of an improvement in the maps' update frequency. Additionally, the results should benefit the large agricultural community through the reduction of routine soil sampling cost and improved prediction accuracy.

1. Introduction

Rainfed agroecosystems occupy 80 million ha in arid, semi-arid, and sub-humid climate zones in India, constituting nearly 57% of the cultivated area (Srinivasarao et al., 2013b). Soil plays a pivotal role for grain output because it impacts crop growth, nutrient holding/leaching patterns, water requirements, and overall health of the soil-crop-hydrology continuum. Sustainable soil management can help reduce the risk of soil degradation and improve the food security status of indigenous farmers in poor rural smallholder farm settings in the long term. Digital Soil Mapping (DSM) is an update-to-date technique that can utilize remote sensing, geostatistics and data mining techniques to predict soil properties across various spatial and temporal scales (McBratney et al., 2003), and it has high potential to help smallholder farmers develop sustainable soil management schemes, and increase food security and soil security.

* Corresponding author at: School of Natural Resource and Environment, University of Florida, 103 Black Hall, PO Box 116455, Gainesville, FL 32611, USA.
E-mail addresses: xuyimi@ufl.edu (Y. Xu), sesmith@ufl.edu (S.E. Smith), sabgru@ufl.edu (S. Grunwald), aamr@ufl.edu (A. Abd-Elrahman), s.wani@cgiar.org (S.P. Wani).

http://dx.doi.org/10.1016/j.isprsjprs.2016.11.001
0924-2716/

Remote sensing images allow derivation of biophysical properties relevant for crop growth and soil conditions at different scales covering large regions (Marshall and Thenkabail, 2015; Wang et al., 2016). Spectral indices derived from remote sensing images become an important source of environmental variables in digital soil mapping with limited data (McBratney et al., 2003). Due to the limitation of relatively low spatial resolution, some multispectral images are too coarse to identify ground features and provide spectral information required in fine scale geoscientific research. Some operating earth observation satellites such as Landsat 8, WorldView-3, and SPOT have a panchromatic band that provides higher spatial resolution compared with multispectral bands. Image fusion, a classical remote sensing technique, is the combination of two or more images to form a new image using certain algorithm (Van and Pohl, 1994). It is aimed at improving spatial resolution, enhancing structural and textural details, and preserving the spectral reliability of the original multispectral data simultaneously (Zhang, 2010). Ehlers et al. (2010) classified the image fusion methods into three levels: pixel level, feature level, and decision level. Pixel level fusion methods, also called image pan-sharpening methods, are the most frequently used methods for multispectral image fusion (Ehlers et al., 2010; Zhang, 2010). According to Ehlers et al. (2010), pixel level fusion methods can also be divided into three classes. The first class is color-related methods such as the intensity-hue-saturation (IHS) method. The second class is band statistics methods such as the Gram–Schmidt (GS) method. The third class is based on arithmetic operations such as the Brovey method.

Soil prediction maps based on some multispectral indices are too coarse and cannot characterize the micro-variation of soil properties in small scale farmland. The spectral data from pan-sharpened images have the potential to be incorporated in DSM research in fine scale areas, such as smallholder farm settings. Few researchers have utilized image pan-sharpening technique in DSM research. Francés and Lubczynski (2011) utilized QuickBird and aerial orthophoto images to classify soil classes. Vaudour et al. (2013) concluded that pan-sharpened SPOT 5 image spectral has a higher prediction ability for topsoil carbon content than multispectral SPOT 4 image spectral using multiple linear regression bootstrap modeling. Many research also compared different image pan-sharpened methods and their performance. Jalan and Sokhi (2012) showed high-pass filtering (HPF), Gram–Schmidt (GS) and PANSHARP methods produced comparable pan-sharpening images with high spectral quality and spatial enhancement, while Brovey method produced the pan-sharpening images with spatial enhancement but highly distorted radiometry. Karathanassi et al. (2007) compared the 17 image pan-sharpening methods, local mean and variance matching (LMVM), least square fusion (LSF), and GS fusion methods have the highest performance in terms of peak signal-to-noise ratio (PSNR) and photointerpretation results. However, there is no paper comparing the effects of different pan-sharpened spectral indices on soil prediction models. The relationship between soil properties and spectral indices from pan-sharpened (PAN) images, and the effects of spectral indices from PAN images on soil prediction models have rarely been explored before.

Soil nitrogen depletion (Chander et al., 2014; Sahrawat et al., 2010), and soil potassium depletion (Bhattacharyya et al., 2006; Srinivasarao et al., 2013a) constrain the enhancing grain production in smallholder farms in South India. There is few DSM research incorporating environmental variables such as spectral indices to characterize soil nutrients in South India. To analyze the effects of image pan-sharpening on DSM, this research 1) fused the panchromatic band and multispectral bands of WorldView-2, GeoEye-1, and Landsat 8 images using Brovey, Gram-Schmidt (GS), and Intensity-Hue-Saturation (IHS) methods; 2) analyzed the relationships between soil properties (total nitrogen (TN) and exchangeable potassium (K_{ex})) and various PAN and MS remote sensing spectral indices; and 3) assessed the effects of the incorporation of selected PAN spectral indices on soil prediction models.

2. Materials and methods

2.1. Study area description

Kothapally (latitude 17°20′ to 17°24′N and longitude 78°5′ to 78°8′E, elevation 600–640 m) is a smallholder village located in Ranga Reddy District, Telangana State of India. It is nearly 40 km from the International Crops Research Institute for the Semi-Arid Tropics (ICRISAT) Center, and 74 km distance from the city of Hyderabad. The village of Kothapally is characterized by an undulating topography with an average slope of 2.5%. The Vertisols and associated soils make up 90% of the area. The annual rainfall is 802 mm (1999–2008) and soil depth ranges from 30 to 120 cm (Sreedevi et al., 2004). In the rainy season, the main cropping systems are cotton (*Gossypium hirsutum*) and rice (*Oryza sativa*). In the dry season, sorghum (*Sorghum bicolar*) is the predominant crop type. Major crop rotation is cotton-sorghum and cotton-tomato in the rainy-dry season. According to Sreedevi et al. (2004), there are 274 households composed of 1493 people in the village, and the average landholding per household is 1.4 ha. Smallholder farmers in the village utilized ground water to irrigate the crops (Sreedevi et al., 2004). The application of chemical fertilizers, pesticides and other agricultural input is not common in the village due to the limited financial resources of smallholder farmers (Wani et al., 2003).

2.2. Field sampling and laboratory analysis

A total of 255 soil samples at 0–15 cm in Kothapally were collected by ICRISAT and University of Florida Team in May 2012 (Fig. 1). Site-specific descriptions, including landform, crop types, and soil color, as well as x and y coordinates, were recorded at each sampling point. Each soil sampling location was measured by a Differential Global Positioning System (DGPS) with sub-meter accuracy (Trimble Navigation Ltd., Sunnyvale, California, USA). GPS post-correction was performed by Aimil Ltd. (www.aimil.com) located in Hyderabad, India. After being air-dried for one week, the soil samples from the study area were then sieved using a 2-mm sieve before being stored in plastic bags for future analysis. All the soil samples were analyzed by ICRISAT, for soil total nitrogen (TN) (Krom, 1980), and exchangeable potassium (K_{ex}) (Thomas, 1982). Results for soil TN and K_{ex} were reported on a concentration basis (mg kg^{-1}).

2.3. Remote sensing data

Two MS Landsat 8 images, one WorldView-2 image, one GeoEye-1 image in Kothapally were collected (Table 1). The Advanced Spaceborne Thermal Emission and Reflection Radiometer (ASTER) Digital Elevation Model (DEM) from the United States Geological Survey (USGS) website (http://earthexplorer.usgs.gov) was also collected. Those images were all collected from dry season. Multiple spectral indices were extracted from those remote sensing images.

2.4. Image pan-sharpening

This research fused the panchromatic band and multispectral bands of WorldView-2, GeoEye-1, and Landsat 8 in Kothapally. Three major image pan-sharpening techniques including Brovey methods (Tu et al., 2001), intensity-hue-saturation (IHS) (Kalpoma and Kudoh, 2007), and Gram–Schmidt (GS) (Laben and

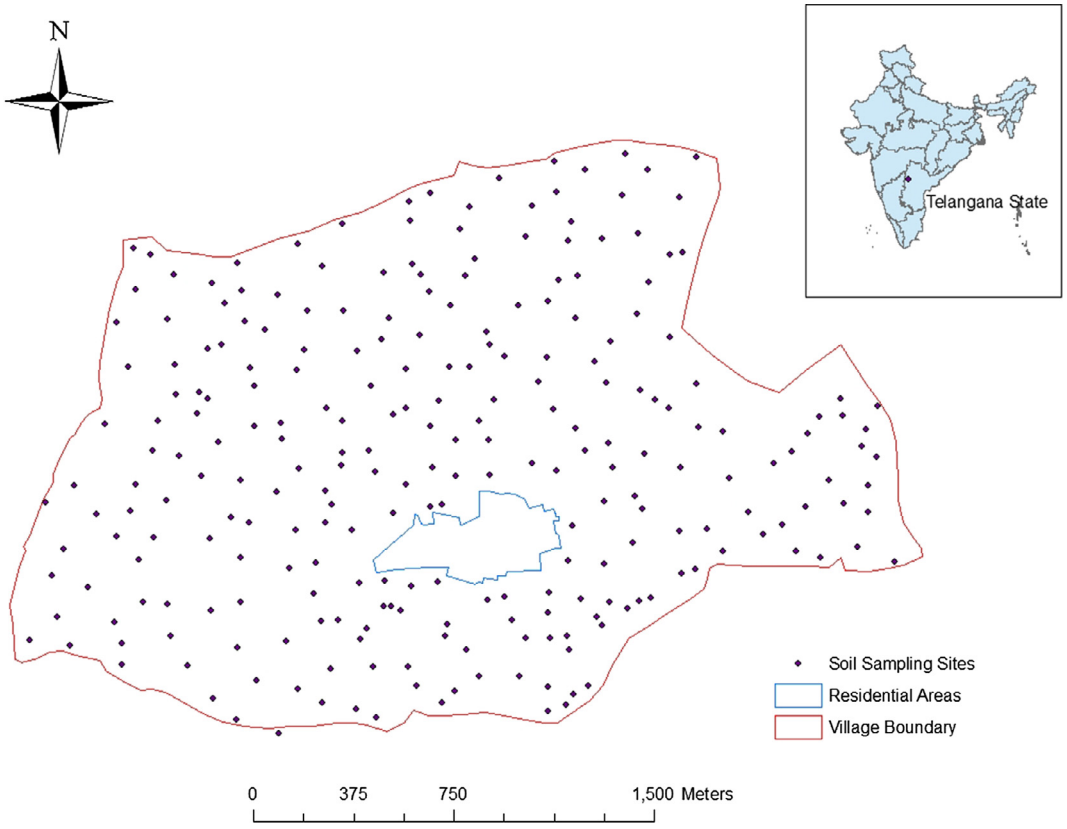

Fig. 1. The boundary and soil samplings of Kothapally Village.

Table 1
Remote sensing images utilized in the research.

Remote sensing images (acquisition date)	Abbreviation
Landsat 8 MS image (2013-4-13)	LTa
Landsat 8 Brovey PAN image (2013-4-13)	LTaB
Landsat 8 GS PAN image (2013-4-13)	LTaG
Landsat 8 IHS PAN image (2013-4-13)	LTaI
Landsat 8 MS image (2013-4-29)	LTb
Landsat 8 Brovey PAN image (2013-4-29)	LTbB
Landsat 8 GS PAN image (2013-4-29)	LTbG
Landsat 8 IHS PAN image (2013-4-29)	LTbI
WorldView-2 MS image (2011-12-14)	WV
WorldView-2 Brovey PAN image (2011-12-14)	WVB
WorldView-2 GS PAN image (2011-12-14)	WVG
WorldView-2 IHS PAN image (2011-12-14)	WVI
GeoEye-1 image (2012-1-21)	GE
GeoEye-1 Brovey PAN image (2012-1-21)	GEB
GeoEye-1 GS PAN image (2012-1-21)	GEG
GeoEye-1 IHS PAN image (2012-1-21)	GEI

Abbreviations: PAN, pan-sharpened; MS, multispectral; GS, Gram–Schmidt; IHS, intensity hue saturation.

Brower, 2000) were utilized to perform the image pan-sharpening between the multispectral and panchromatic images. Image pan-sharpening was performed in the ENVI software (version 5.0, Exelis Visual Information Solutions, Boulder, Colorado). All the PAN images (Table 1) have four bands: blue, green, red, and near infrared.

2.4.1. Brovey method

The Brovey method preserves the relative spectral contributions of each pixel and replaces its overall brightness with the high-resolution panchromatic band (Tu et al., 2001). Each multispectral band is resampled to the panchromatic band spatial resolution, divided by the sum of the all the multispectral image intensities and then multiplied with the corresponding panchromatic image intensity (Ehlers et al., 2010). The Brovey method is given by

$$MS_{high} = MS_{low} * \left(\frac{Pan}{I}\right) \quad (1)$$

where MS_{high} is the pixel value of the pan-sharpened image; MS_{low} is the pixel value of MS image; *Pan* is the pixel value of panchromatic band; *I* is the value of intensity, which is the average value of blue, green, and red bands.

2.4.2. Gram-Schmidt (GS) method

The Gram-Schmidt pan-sharpening method is based on Gram-Schmidt (GS) orthogonalization. GS orthogonalization is performed to orthogonalize matrix data or bands of a digital image (Laben and Brower, 2000). It removes the redundant or correlated information contained in multiple remote sensing image bands, and produces a new set of orthogonal and linear independent bands (Laben and Brower, 2000). It first created a simulated low resolution panchromatic band as a weighted linear combination of multispectral bands. Then GS orthogonalization is performed using all the bands including the simulated panchromatic band and the multispectral bands, and the simulated panchromatic band is the first band in the GS orthogonalization. After making all bands orthogonal by using the GS orthogonalization, the high spatial resolution panchromatic band replaces the first GS band. Lastly, an inverse GS transform is utilized to create the PAN bands (Ehlers et al., 2010; Laben and Brower, 2000).

2.4.3. Intensity, hue, and saturation (IHS) method

The IHS transform is a color-related technique where RGB space is replaced in the IHS space by intensity (I), hue (H), and saturation (S) level. The intensity is brightness of the remote sensing image, hue is the dominant or average wavelength of the light determined by the relative proportions of R, G, and B colors, and saturation is

the purity of a color (Alparone et al., 2015). First, it converts the RGB space into the IHS space (IHS transform). Second, the value of intensity I (I = (Red + Green + Blue)/3) is replaced by the value of panchromatic band. Third, IHS space is retransformed back into the original RGB space (reverse IHS transform) (Kalpoma and Kudoh, 2007).

2.5. Image processing

The map projection for all the GIS and remote sensing data in the study area is WGS 84/UTM zone 44N. Radiometric calibration was applied to all the original images, and transferred Digital Numbers (DNs) to top-of-atmosphere spectral radiance. Those top-of-

Table 2
Environmental variables from MS and PAN images.

Environmental variables	Abbreviation	References
Coastal band reflectance	Coastal	
Blue band reflectance	Blue	
Green band reflectance	Green	
Yellow band reflectance	Yellow	
Red band reflectance	Red	
Red edge band reflectance	Rededge	
Near Infrared band reflectance	NIR	
Near Infrared band 1 reflectance	NIR1	
Near Infrared band 2 reflectance	NIR2	
Short Wavelength band 1 reflectance	SWIR1	
Short Wavelength band 2 reflectance	SWIR2	
Green/Blue ratio	GB	
Red/Blue ratio	RB	
Red/Green ratio	RG	
Red edge/Blue ratio	REB	
Red edge/Green ratio	REG	
Red edge/Red ratio	RER	
NIR/Blue ratio	NB	
NIR/Green ratio	NG	
NIR/Red ratio	NR	
NIR1/Blue ratio	N1B	
NIR1/Green ratio	N1G	
NIR1/Red ratio	N1R	
NIR1/Red edge ratio	N1RE	
NIR2/Blue ratio	N2B	
NIR2/Green ratio	N2G	
NIR2/Red ratio	N2R	
NIR2/Red edge	N2RE	
NIR2/NIR1 ratio	N2N1	
SW1/Blue ratio	S1B	
SW1/Green ratio	S1G	
SW1/Red ratio	S1R	
SW1/NIR ratio	S1N	
SW2/Blue ratio	S2B	
SW2/Green ratio	S2G	
SW2/Red ratio	S2R	
SW2/NIR ratio	S2N	
SW2/SW1 ratio	S2S1	
Normalized Difference Vegetation Index	NDVI	Rouse et al. (1974)
Normalized Difference Green Index	NDVIg	Gitelson et al. (1996)
Simple Ratio	SR	Cohen (1991)
Transformed Spectral Index	TVI	Nellis and Briggs (1992)
Green Chlorophyll Index	CIg	Gitelson et al. (2005)
Soil Adjusted Vegetation Index	SAVI	Qi et al. (1994)
Atmospherically Resistant Vegetation Index	ARVI	Kaufman and Tanré (1996)
Crust Index	CI	Karnieli (1997)
Modified Chlorophyll Absorption in Reflectance Index	MCARI	Daughtry et al. (2000)
Red-edge Chlorophyll Index	CIr	Gitelson et al. (2005)
Normalized Difference Red-edge Index	NDVIr	Gitelson and Merzlyak (1994), Sims and Gamon (2002)
Transformed Chlorophyll Absorption in Reflectance Index	TCARI	Haboudane et al. (2002)
Moisture Stress Index	MSI	Rock et al. (1986)
Normalized Difference Water Index	NDWI	Gao (1996)
Mid-infrared Index	MidIR	Musick and Pelletier (1988)
Bare soil index	BSI	Rikimaru and Miyatake (1997)
Normalized Difference Soil Index	NDSI	Rogers and Kearney (2004)
At-satellite brightness temperature for band 10 (10.30–11.30 μm) (K)	T1	
At-satellite brightness temperature for band 11 (11.50–12.50 μm) (K)	T2	
Elevation (m)	Elevation	
Aspect (Degree)	Aspect	
Flow Accumulation	FlowAccu	
Flow Direction	FlowDir	
Slope (Degree)	Slope	
The first principal component score	PC1	
The second principal component score	PC2	
The third principal component score	PC3	
The fourth principal component score	PC4	
The fifth principal component score	PC5	

Table 3
Descriptive analysis of total nitrogen (TN) and exchangeable potassium (K_{ex}).

Soil property	Data Type	N	Mean	Median	SD	Min	Max	Range	Skew	Kurtosis	CV
TN (mg kg^{-1})	Total	255	868.79	855.75	220.57	328.8	1820.7	1491.91	0.47	1.05	0.25
	Calibration	179	874.18	855.75	222.21	399.9	1820.7	1420.81	0.63	1.37	0.25
	Validation	76	856.09	860.32	217.49	328.8	1507.0	1178.18	0.06	−0.02	0.25
K_{ex} (mg kg^{-1})	Total	255	241.64	231.06	110.01	54.86	614.75	559.90	0.65	0.13	0.46
	Calibration	179	241.92	228.69	107.76	54.86	614.75	559.90	0.64	0.07	0.45
	Validation	76	241.00	231.98	115.87	59.94	606.53	546.59	0.66	0.11	0.48

Abbreviations: N, number of samples; SD, standard deviation; CV, coefficient of variation.

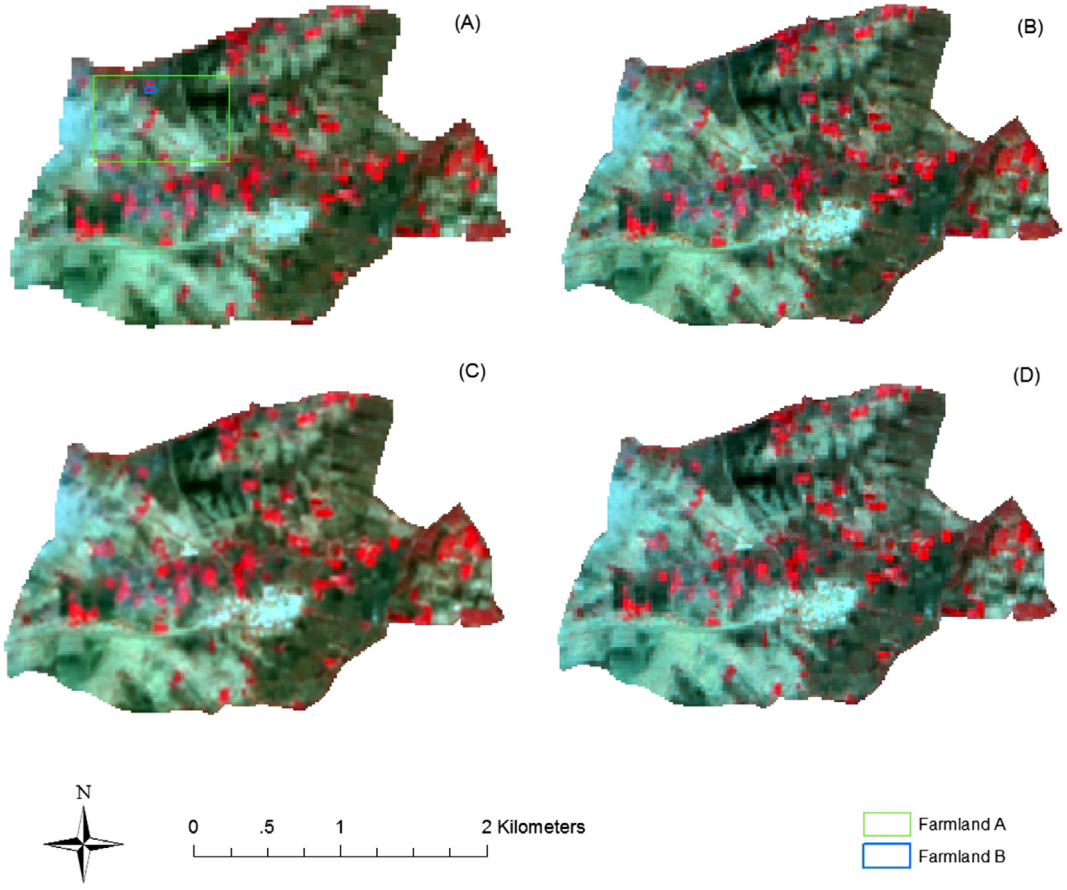

Fig. 2. MS and PAN Landsat 8 images (2013-4-13) of Kothapally. (A) MS Landsat 8 image; (B) Brovey PAN Landsat 8 Image; (C) Gram–Schmidt (GS) PAN Landsat 8 image; (D) Intensity-Hue-Saturation (IHS) PAN Landsat 8 image.

atmosphere spectral radiance images were converted to surface reflectance using the Fast Line-of-Site Atmospheric Analysis of Spectral Hypercubes (FLAASH) tool in the ENVI software (version 5.0, Exelis Visual Information Solutions, Boulder, Colorado). The geometric correction of all the images were performed with the 14 control points collected by a Differential Global Positioning System (DGPS) with sub-meter accuracy. The nearest neighborhood method was used to resample all the images in the geometric correction. The Root Mean Square Error (RMSE) was smaller than 0.5 pixel for each remote sensing image.

2.6. Environmental variables extraction

Topographic attributes such as elevation, slope, aspect, flow direction, and flow accumulation were extracted from the ASTER Global DEM dataset using the ArcGIS 10.1 (ESRI, 2011). Geographic attributes of each soil sampling point such as x, y coordinates in Universal Transverse Mercator projection were collected by the same GPS techniques used for the control point collection. Several environmental variables such as band reflectances, band ratios, vegetation indices, principal component of remote sensing bands were extracted from remote sensing images. Environmental variables from all the multispectral (MS) and pan-sharpened (PAN) images were shown in Table 2.

2.7. Relationship between soil properties and environmental variables

Spearman's rank correlation coefficients between soil properties (TN and K_{ex}) and environmental variables were calculated. The Boruta algorithm based on random forest (RF) method (Rudnicki and Kursa, 2010) can cope with redundancy and collinearity between the variables (Hitziger and Ließ, 2014; Xiong et al., 2014), and it was applied to identify the environmental variables which were relevant to soil TN and K_{ex}.

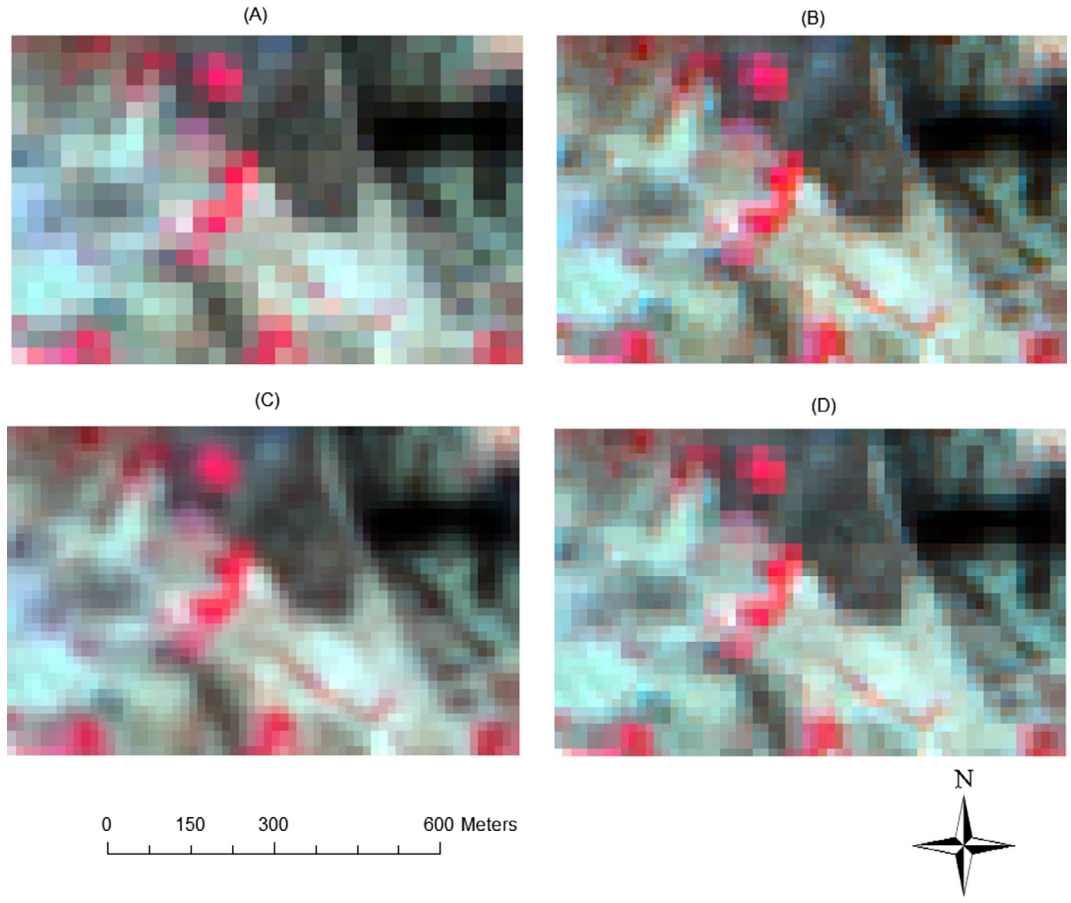

Fig. 3. MS and PAN Landsat 8 images (2013-4-13) of Farmland A in Kothapally. (A) MS Landsat 8 image; (B) Brovey PAN Landsat 8 Image; (C) GS PAN Landsat 8 image; (D) IHS PAN Landsat 8 image.

2.8. Random forest

Random Forest (RF) is a tree-based model for classification or regression (Breiman, 2001). It creates multiple trees using a different bootstrap sample of the data. Each node in RF is split using the best among a subset of predictors randomly chosen at that node (Liaw and Wiener, 2002). RF method was widely applied in remote sensing research (Lopatin et al., 2016) and Digital Soil Mapping research (Heung et al., 2014). After identifying the relevant variables of soil properties by Boruta algorithm, those relevant variables were incorporated as environmental variables into the RF models to predict the soil properties in the study area. Several R packages such as the "Boruta", "randomForest", "rgdl", and "raster" packages (https://cran.r-project.org/web/packages/) were used in the model establish and soil mapping.

2.9. Accuracy of soil prediction models

All the 255 soil sample points were randomly split into calibration set (70%, n = 179) for model calibration and validation set (30%, n = 76) for model validation. The Kolmogorov-Smirnov test (Wang et al., 2003) was applied on soil calibration and validation datasets to ensure they have the same distribution. The coefficient of determination (R^2), root mean squared error (RMSE), residual prediction deviation (RPD), and ratio of performance to inter-quartile distance (RPIQ) (Williams and Norris, 1987) were computed using the R software and used to compare different models.

3. Results

3.1. Descriptive statistics of soil properties

TN measured in 255 soil samplings showed positive skewed distribution with a mean of 868.79 mg kg^{-1}, a median of 855.75 mg kg^{-1}, and a range of 1491.91 mg kg^{-1}. K_{ex} measured in 255 soil samplings also showed positive skewed distribution with a mean of 241.64 mg kg^{-1}, a median of 231.06 mg kg^{-1}, and a range of 559.90 mg kg^{-1}. The descriptive statistics of the calibration and validation sets of both soil properties were similar to those of the whole soil dataset, suggesting both the calibration and validation soil datasets were similar to each other (Table 3).

3.2. Comparison of MS and PAN images

Fig. 2 compared the MS and three PAN Landsat 8 images in Kothapally. All three PAN images had spatial resolutions of 15 m, which showed a stronger capability to identify the vegetation, road, resident settlement, soil and other ground features compared with MS Landsat 8 images. Fig. 3 compared the MS and three PAN Landsat 8 images after zooming to specific area (Farmland A). The linear ground feature (road) in the eastern area of the Farmland A can be identified in Fig. 3(B)–(D), while it is fuzzy in Fig. 3(A). Generally, GS PAN Landsat 8 images have higher spatial quality compared with other PAN Landsat 8 images from visual analysis.

The MS and three PAN WorldView-2 images all showed significant capability in characterizing the ground feature of smallholder farm settings (Fig. 4). The outline of the resident settlement, the

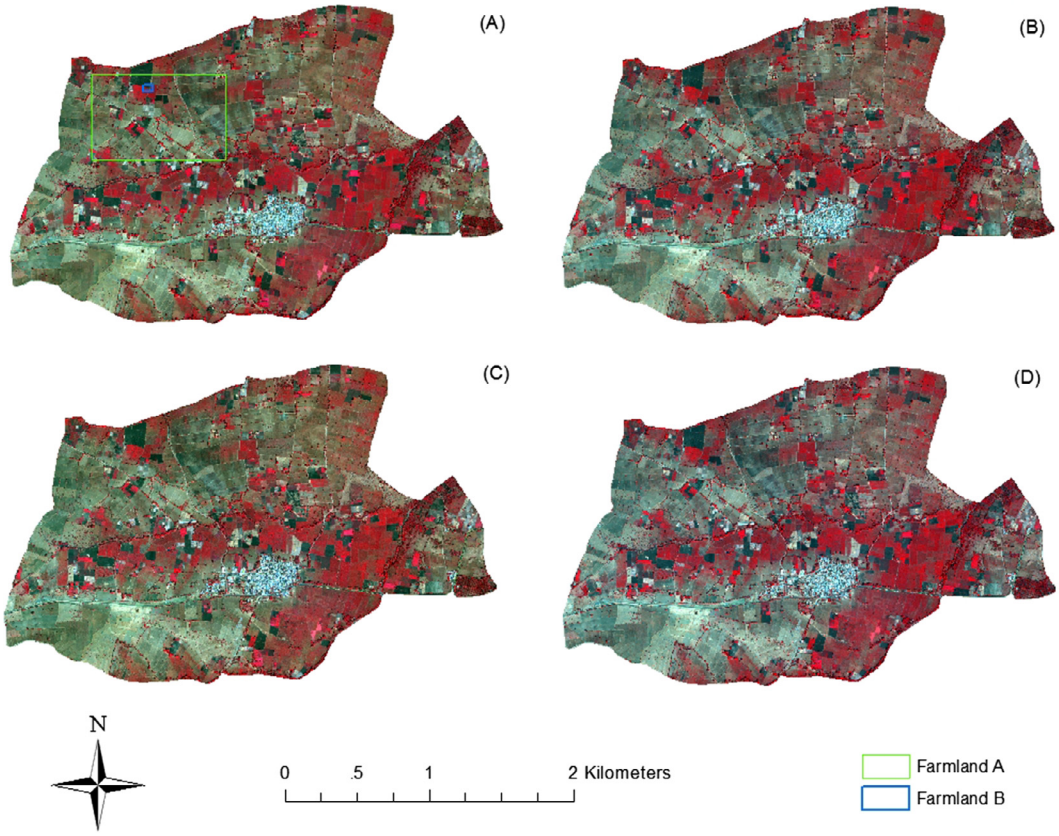

Fig. 4. MS and PAN WorldView-2 images (2011-12-14) of Kothapally. (A) MS WorldView-2 image; (B) Brovey WorldView-2 image; (C) GS WorldView-2 image; (D) IHS WorldView-2 image.

trees between the field blocks, wells, ridges, roads, crop residues, and the color gradients of soil and vegetation can be clearly identified by MS and PAN WorldView-2 images. Fig. 5 compared the MS and three PAN WorldView-2 images in a close up view to an area (named Farmland B). The structural and textural details of ground feature in field block and road junction in MS and PAN WorldView-2 images can be differentiated in Fig. 5. In all, MS and three PAN images all can show the crops in the southwestern and eastern area of Farmland B and the bare soil in the northwestern area of Farmland B. The pathway and road junction between the field blocks in the MS WorldView-2 image (spatial resolution: 2 m), Brovey and IHS PAN images (spatial resolution: 0.5 m) are relatively fuzzy and cannot be identified very clearly. GS PAN WorldView-2 image has a stronger ability to characterize the texture and spatial variability of the crops, and the boundary between pathway and farmland compared with other images. Compared with MS image (Fig. 5(A)), the color distortion of GS PAN image (Fig. 5(C)) is also smaller than Brovey (Fig. 5(B)) and IHS (Fig. 5 (D)) PAN images from visual analysis. As a result, GS PAN WorldView-2 image has higher spatial quality and less color distortion than Brovey and IHS PAN WorldView-2 images.

3.3. Incorporation of pan-sharpened spectral indices into soil TN models

3.3.1. Relationship between TN and spectral indices from MS and PAN Landsat 8 images

Table 4 demonstrated the Spearman's rank correlation coefficients between spectral indices from Landsat 8 images and soil TN. After the incorporation of PAN Landsat 8 spectral indices, more spectral indices had a correlation coefficient greater than 0.4 in absolute terms with soil TN. Red band reflectance, Crust Index (CI), band ratios of red to green (RG), and red to blue (RB) from Brovey PAN Landsat 8 image showed stronger linear correlations with soil TN than any other spectral indices. RG and RB from three PAN images all had relatively strong negative linear relationships with soil TN. CI and Atmospherically Resistant Vegetation Index (ARVI) from all PAN Landsat 8 images showed relative strong positive correlations with TN. Normalized difference vegetation index (LTaINDVI) and Simple Ratio (LTaISR) from IHS PAN image also had relatively strong positive linear correlations with soil TN. The spectral indices of MS Landsat 8 images identified as relevant variables by Boruta algorithm in Table 5 were more diverse compared with those in Table 4. At-satellite brightness temperature for band 10 (T1) and band 11 (T2) of Landsat 8 had very high importance scores with TN. RG, RB, ARVI, and CI from the three PAN images were all identified as relevant variables. More Brovey PAN Landsat 8 image spectral indices (10) were identified as relevant variables with TN compared with GS and IHS PAN Landsat 8 image spectral indices.

3.3.2. Relationship between TN and spectral indices from MS and PAN WorldView-2 and GeoEye-1 images

CI, RB, and red band reflectances of MS GeoEye-1 image had stronger correlations with soil TN than any other spectral indices in Table 6, indicating the correlations between TN and PAN WorldView-2/GeoEye-1 spectral indices were not necessarily always higher than MS WorldView-2/GeoEye-1 spectral indices. The ratios between visible bands, and band reflectances from PAN WorldView-2/GeoEye-1 images had relatively strong negative correlations with soil TN (Table 6). In Table 7, the importance score of RB and CI from MS GeoEye-1 images were larger than any PAN

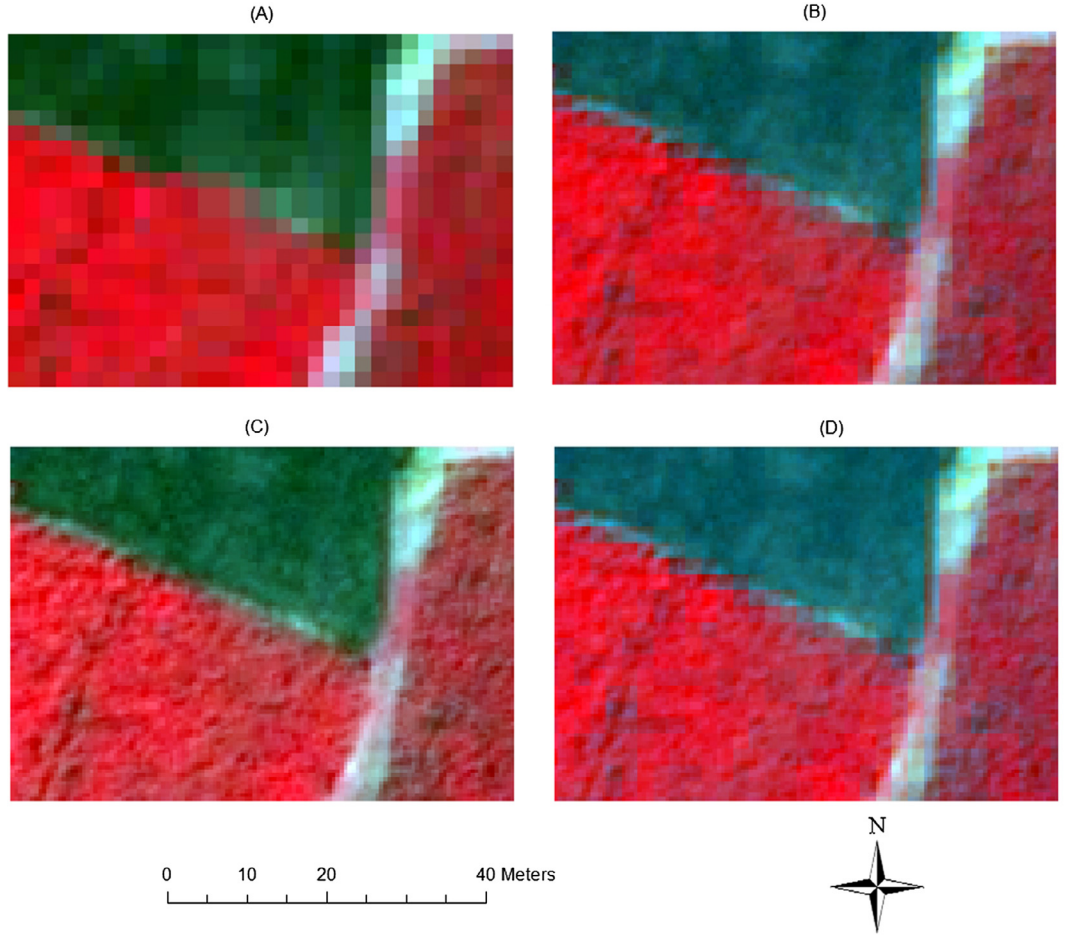

Fig. 5. MS and PAN WorldView-2 images (2011-12-14) of Farmland B in Kothapally. (A) MS WorldView-2 image; (B) Brovey PAN WorldView-2 Image; (C) GS PAN WorldView-2 image; (D) IHS PAN WorldView-2 image.

Table 4
Linear correlations between soil TN and environmental variables extracted from PAN and MS Landsat 8 images.

MS images		MS and Brovey PAN images		MS and GS PAN images		MS and IHS PAN images	
Variable	R	Variable	R	Variable	R	Variable	R
LTbRG	−0.419	LTaBRed	−0.456	LTbGARVI	0.435	LTbIRG	−0.428
LTbARVI	0.409	LTaBCI	0.453	LTbGRG	−0.421	LTaIARVI	0.421
LTaARVI	0.397	LTaBRB	−0.453	LTbRG	−0.419	LTbRG	−0.419
LTbCI	0.390	LTaBRG	−0.453	LTaGARVI	0.411	LTbIARVI	0.414
LTbRB	−0.390	LTbBRG	−0.426	LTbARVI	0.409	LTbARVI	0.409
LTaRG	−0.373	LTaBARVI	0.424	LTaGRG	−0.404	LTbICI	0.408
LTbT2	−0.373	LTbRG	−0.419	LTbGCI	0.399	LTbIRB	−0.408
LTbT1	−0.368	LTbBCI	0.410	LTbGRB	−0.399	LTaIRG	−0.403
LTbPCA5	0.367	LTbBRB	−0.410	LTaARVI	0.397	LTaARVI	0.397
LTaCI	0.364	LTbARVI	0.409	LTaGCI	0.391	LTaICI	0.392
LTaRB	−0.364	LTbBARVI	0.401	LTaGRB	−0.391	LTaIRB	−0.392
LTbRed	−0.353	LTaARVI	0.397	LTbCI	0.390	LTbCI	0.390
LTaRed	−0.339	LTbCI	0.390	LTbRB	−0.390	LTbRB	−0.390
LTbBSI	−0.318	LTbRB	−0.390	LTaGRed	−0.374	LTaINDVI	0.387
LTaT1	−0.309	LTaRG	−0.373	LTaRG	−0.373	LTaISR	0.387

Nomenclature of the variable in Table 4: Remote sensing image (Abbreviation in Table 1) + Spectral index (Abbreviation in Table 2).
Abbreviations: R, Spearman's rank correlation coefficient; GS, Gram-Schmidt; IHS, intensity, hue and saturation.

spectral indices. More GS PAN WorldView-2/GeoEye-1 spectral indices (9) were identified as relevant variables compared with Brovey and IHS PAN WorldView-2/GeoEye-1 spectral indices.

3.3.3. Spatial characteristics of soil TN by different soil prediction models

Table 8 describes eight soil TN prediction models based on the relevant spectral indices identified in Tables 5 and 7. Fig. 6 shows the spatial patterns of TN in Kothapally by models NLTM, NLTB, NLTG, and NLTI based on Landsat 8 spectral indices. Four maps in Fig. 6 demonstrated similar spatial pattern, as spectral libraries in four models include some identical MS spectral indices. The southwestern and northern areas of the village were low in TN. The east-west strip areas in the center of the village and the south-eastern area of the village were high in TN. Soil TN maps based on MS/PAN Landsat 8 spectral indices (Fig. 6(B)–(D)) have higher

Table 5
Importance score (mean Z-score) between soil TN and relevant variables extracted from PAN and MS Landsat 8 images identified by the Boruta algorithm.

MS images		MS and Brovey PAN images		MS and GS PAN images		MS and IHS PAN images	
Variable	MeanZ	Variable	MeanZ	Variable	MeanZ	Variable	MeanZ
LTbRG	13.33	LTbBRG	11.45	LTbT1	11.78	LTbIRG	12.13
LTbT1	12.07	LTbT1	9.64	LTbGARVI	9.27	LTbIARVI	12.12
LTbARVI	10.89	LTaBRed	8.72	LTbRG	8.99	LTbT1	11.67
LTbT2	9.13	LTbBARVI	8.11	LTbT2	8.39	LTbT2	7.94
LTbRB	7.89	LTaBRG	8.02	LTaGRB	7.84	LTbIRB	7.79
LTbPCA5	7.73	LTbBRB	6.96	LTbARVI	7.76	LTaIARVI	7.51
LTaARVI	7.42	LTbT2	6.79	LTbGRG	6.93	LTbICI	6.64
LTbCI	7.15	LTbBRed	6.71	LTaGCI	6.90	LTaPCA5	6.18
LTaPCA5	6.93	LTaPCA5	6.49	LTaGARVI	6.61	LTbRG	6.14
LTbGB	6.86	LTaBRB	6.43	LTbPCA5	6.30	LTbARVI	5.77
LTbPCA3	5.96	LTbRG	6.30	LTbGRB	6.19	LTbPCA5	5.76
LTaRB	5.94	LTbBCI	6.01	LTbGGB	6.06	LTbINDVI	4.89
LTbRed	5.65	LTbPCA3	5.90	LTaPCA5	5.56		
LTaT1	5.39	LTaBCI	5.72	LTbGCI	5.41		
		LTaBARVI	5.38				

Nomenclature of the variable in Table 5: Remote sensing image (Abbreviation in Table 1) + Spectral index (Abbreviation in Table 2).
Abbreviation: MeanZ, importance score; GS, Gram-Schmidt; IHS, intensity, hue and saturation.

Table 6
Linear correlations between soil TN and environmental variables extracted from PAN and MS WorldView-2 and GeoEye-1.

MS image		MS and Brovey PAN images		MS and GS PAN images		MS and IHS PAN images	
Variable	R	Variable	R	Variable	R	Variable	R
GECI	0.475	GECI	0.475	GECI	0.475	GECI	0.475
GERB	−0.475	GERB	−0.475	GERB	−0.475	GERB	−0.475
GERed	−0.474	GERed	−0.474	GERed	−0.474	GERed	−0.474
GERG	−0.440	GEBRed	−0.456	GEGRG	−0.456	GEIRed	−0.457
GEBlue	−0.395	GEBCI	0.453	GEGARVI	0.452	GEICI	0.455
WVCI	0.393	GEBRB	−0.453	GEGCI	0.446	GEIRB	−0.455
WVRB	−0.393	GEBRG	−0.453	GEGRB	−0.446	GEIRG	−0.453
GEGreen	−0.390	GERG	−0.440	GERG	−0.440	GERG	−0.440
GEPCA2	−0.381	GEBARVI	0.424	GEGRed	−0.437	GEIARVI	0.426
WVRG	−0.372	GEBlue	−0.395	GEBlue	−0.395	GEBlue	−0.395
WVPCA4	0.354	WVCI	0.393	WVCI	0.393	WVCI	0.393
GEARVI	0.351	WVRB	−0.393	WVRB	−0.393	WVRB	−0.393
WVRed	−0.325	GEGreen	−0.390	GEGreen	−0.390	GEGreen	−0.390
WVYellow	−0.318	GEPCA2	−0.381	GEGGreen	−0.388	GEIBlue	−0.382
GENDVI	0.262	WVRG	−0.372	GEGBlue	−0.388	GEPCA2	−0.381

Nomenclature of the variable in Table 6: Remote sensing image (Abbreviation in Table 1) + Spectral index (Abbreviation in Table 2).

Table 7
Importance score (mean Z-score) between soil TN and relevant variables extracted from PAN and MS WorldView-2 and GeoEye-1 identified by the Boruta algorithm.

MS image		MS and Brovey PAN images		MS and GS PAN images		MS and IHS PAN images	
Variable	MeanZ	Variable	MeanZ	Variable	MeanZ	Variable	MeanZ
GERB	12.85	GERB	11.95	GERB	11.18	GERB	11.75
GERed	11.20	GECI	10.19	GECI	9.76	GECI	10.17
GECI	11.08	GERed	10.03	GEGRed	9.47	GERed	9.87
WVPCA4	9.40	WVPCA4	9.55	GERed	9.05	WVPCA4	9.64
GERG	8.00	GEBRed	8.02	WVPCA4	8.44	GEIRed	8.75
GEGreen	7.66	GERG	7.22	GEGRG	7.67	GEINIR	7.49
GESAVI	6.02	GEGreen	6.75	GEGRB	7.51	GERG	7.24
WVRB	5.80	GEBNIR	6.64	GEGARVI	7.25	GEGreen	7.03
WVCI	5.58	GESAVI	5.97	GERG	7.21	GESAVI	6.31
WVPCA3	5.55	GEBRG	5.77	GEGCI	6.49	GEIRG	6.00
GEBlue	5.36	WVRB	5.55	WVGRG	6.44	GEIRB	5.79
GEPCA2	5.29	GEBRB	5.24	GESAVI	5.88	WVCI	5.71
				GEGreen	5.85	WVIRed	5.63
				WVGCI	5.71		
				WVGRB	5.70		
				WVGRed	5.54		

Nomenclature of the variable in Table 7: Remote sensing image (Abbreviation in Table 1) + Spectral index (Abbreviation in Table 2).

capability to discern the variation of TN in fine spatial resolution compared with soil TN map based MS Landsat 8 spectral indices (Fig. 6(A)). Soil TN maps by model NLTB (Fig. 6(B)) and NLTI (Fig. 6(D)) showed smoother spatial variation of TN than soil TN map by model NLTG (Fig. 6(C)).

Four maps in Fig. 7 demonstrated similar spatial patterns of TN as those in Fig. 6. However, the variability and complexity of TN were much better depicted by four maps in Fig. 7 compared with those in Fig. 6. In Fig. 7, linear pattern showed the low TN in the road, blocky distribution demonstrated the variation of TN in

Table 8
Validation results of different soil TN models.

Model	Adj R^2	RMSE (mg kg^{-1})	RPD	RPIQ	Spectral library	Grid size (m)
NLTM	0.26	186.67	1.17	1.50	14 spectral indices from MS Landsat 8 images in Table 5	30
NLTB	0.35	175.85	1.24	1.60	15 spectral indices from MS and Brovey PAN Landsat 8 images in Table 5	15
NLTG	0.32	180.43	1.22	1.73	15 spectral indices from MS and GS PAN Landsat 8 images in Table 5	15
NLTI	0.31	180.38	1.21	1.56	13 spectral indices from MS and IHS PAN Landsat 8 images in Table 5	15
NWGM	0.32	178.09	1.22	1.58	12 spectral indices from MS WorldView-2 and GeoEye-1 images in Table 7	2
NWGB	0.42	165.66	1.32	1.70	12 spectral indices from MS and Brovey PAN WorldView-2 and GeoEye-1 images in Table 7	0.5
NWGG	0.43	164.67	1.32	1.71	16 spectral indices from MS and GS PAN WorldView-2 and GeoEye-1 images in Table 7	0.5
NWGI	0.36	174.05	1.25	1.61	13 spectral indices from MS and IHS PAN WorldView-2 and GeoEye-1 images in Table 7	0.5

Nomenclature of model name in Table 8: Soil property + Remote sensing image + Image type.
Soil property: N, total nitrogen; Remote sensing image: LT, Landsat 8 images; WG, WorldView-2 and GeoEye-1 images. Image Type: M, multispectral image, B, Brovey image, G, GS image, I, IHS image.

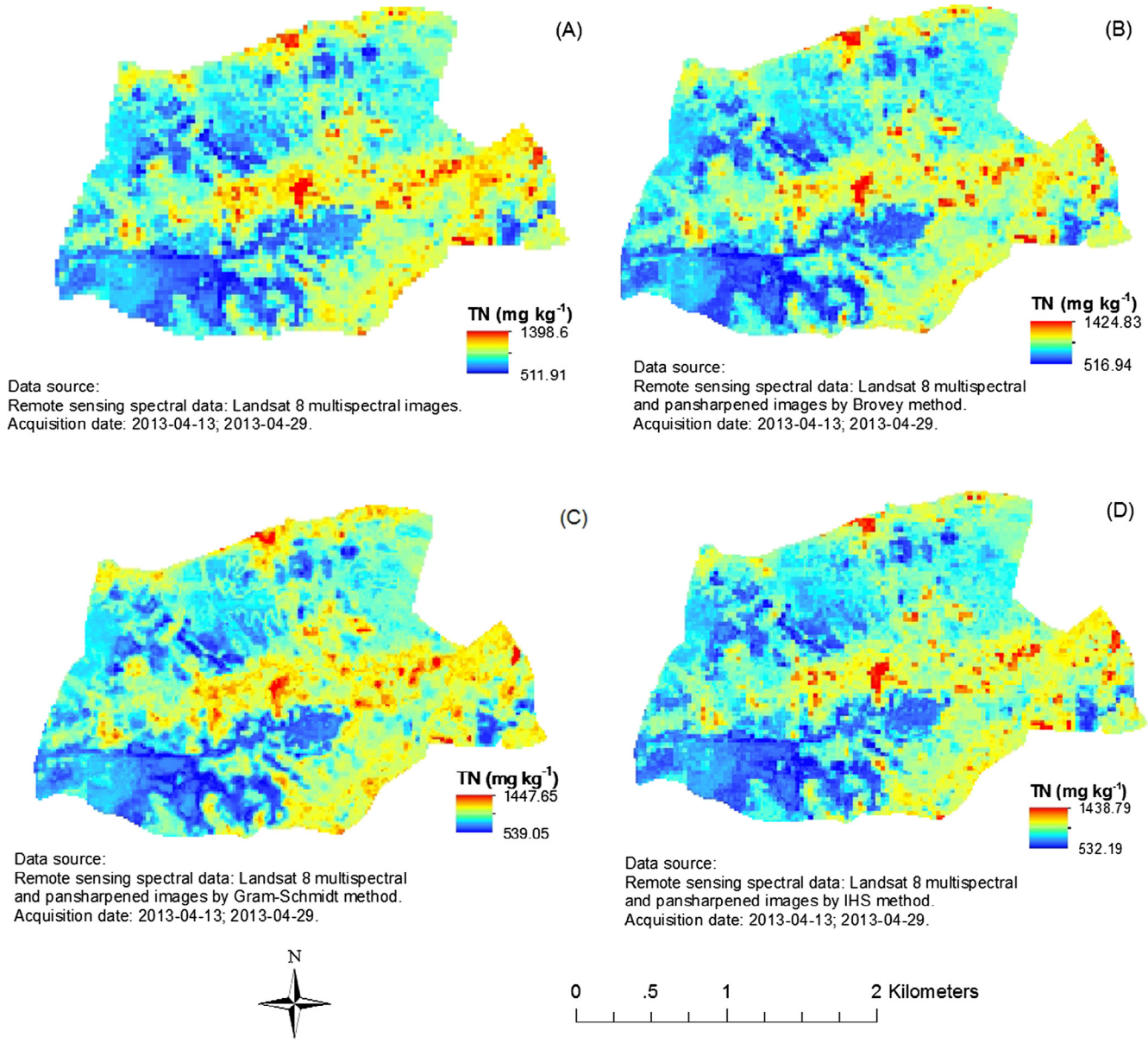

Fig. 6. Soil TN prediction at 0–15 cm depth in Kothapally by (A) model NLTM, (B) model NLTB, (C) model NLTG, (D) model NLTI.

different field blocks, and point pattern illustrated the heterogeneous distribution of TN across the village.

3.3.4. Assessment of soil TN prediction models

Table 8 compared validation results of different soil TN models. Comparing four Landsat 8-based soil TN prediction models, the model fit (Adj R^2) is ordered by NLTB > NLTG > NLTI > NLTM, and the prediction error (RMSE) is ordered by NLTM > NLTG > NLTI > NLTB. Comparing four WorldView-2/GeoEye-1-based soil TN prediction models, the model fit is ordered by NWGG > NWGB > NWGI > NWGM, and the prediction error is ordered by NWGM > NWGI > NWGB > NWGG. Model NWGG

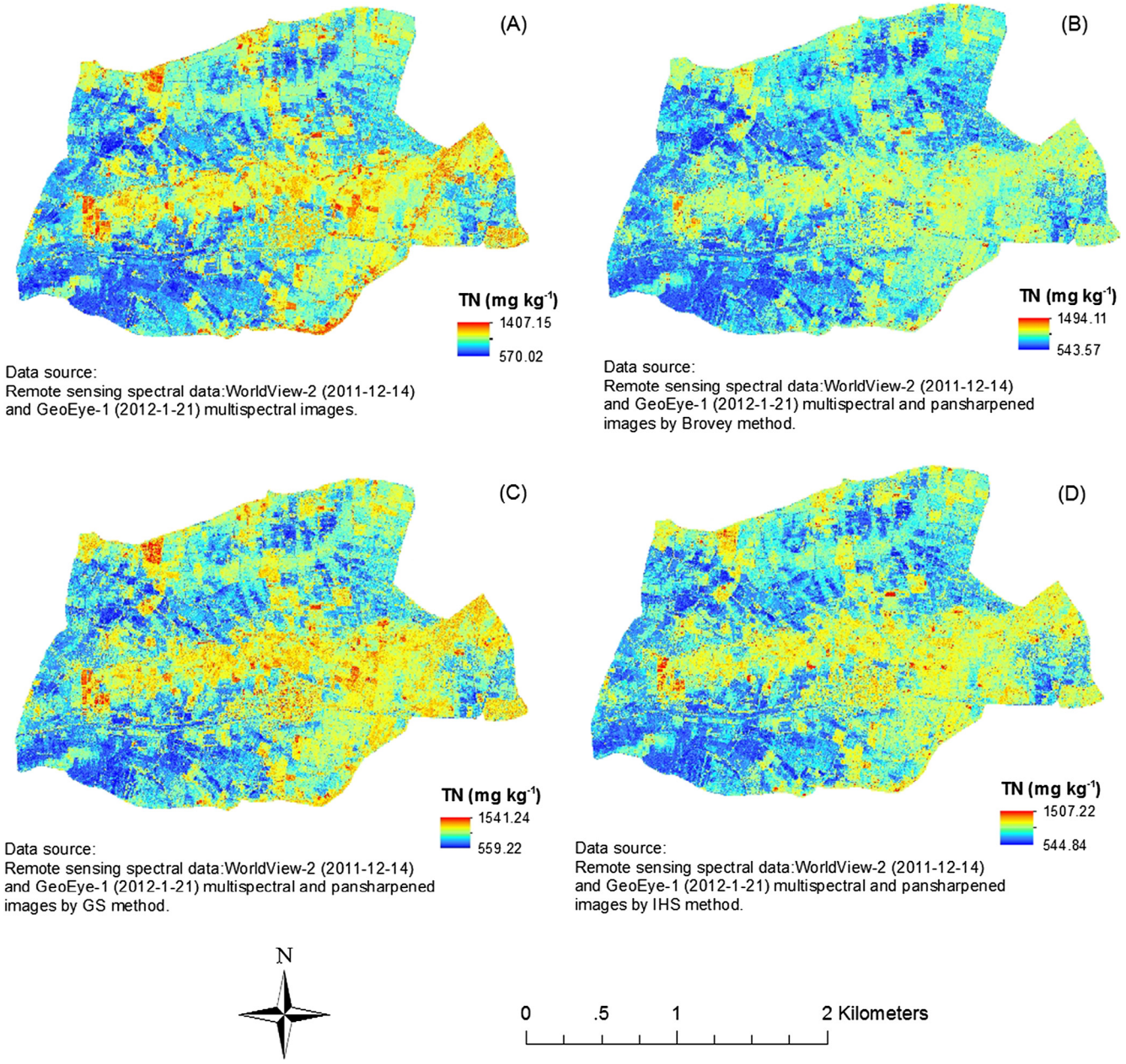

Fig. 7. Soil TN prediction at 0–15 cm depth in Kothapally by (A) model NWGM, (B) model NWGB, (C) model NWGG, (D) model NWGI.

attained the highest model fit (Adj R^2 = 0.43) and lowest prediction error (RMSE = 164.67 mg kg^{-1}) among all models. The results suggested the soil TN prediction models based on spectral libraries incorporating both PAN and MS spectral indices can attain higher model fit and lower prediction error compared with those only incorporating MS spectral indices.

3.4. Incorporation of pan-sharpened spectral indices into soil K_{ex} model

3.4.1. Relationship between soil K_{ex} and spectral indices from MS and PAN Landsat 8 images

Table 9 shows the Spearman's rank correlation coefficients between K_{ex} and spectral indices from Landsat 8 images. GB, RB, the red and green band reflectance from three PAN Landsat 8 images all had relatively strong negative linear relationships with soil K_{ex}. CI from three PAN Landsat 8 images all had relatively strong positive linear correlations with soil K_{ex}. In Table 10, four Brovey PAN spectral indices, eight GS PAN spectral indices, and six IHS PAN spectral indices had higher importance scores with K_{ex} than all the MS spectral indices. It suggested the incorporation of PAN Landsat 8 spectral indices can enhance the prediction capability of soil K_{ex}. Identical spectral index from MS and PAN Landsat 8 images such as LTbBGB and LTbGB, LTbGARVI and LTbARVI, LTbICI and LTbCI were identified as relevant variables simultaneously. More GS PAN spectral indices (12) were identified as relevant variables with K_{ex} compared with other PAN Landsat 8 spectral indices.

3.4.2. Relationship between soil K_{ex} and spectral indices from MS and PAN WorldView-2 and GeoEye-1 images

ARVI from three PAN WorldView-2 images had the highest linear correlations with soil K_{ex} (Table 11). Similar to the characteristics of MS spectral indices, the ratio between visible bands and

Table 9
Linear correlations between soil K_{ex} and environmental variables extracted from PAN and MS Landsat 8 images.

MS image		MS and Brovey PAN images		MS and GS PAN images		MS and IHS PAN images	
Variable	R	Variable	R	Variable	R	Variable	R
LTbGB	−0.537	LTbBGB	−0.565	LTbGGB	−0.545	LTbIGB	−0.564
LTaGB	−0.511	LTbGB	−0.537	LTaGGB	−0.545	LTaIGB	−0.543
LTbGreen	−0.510	LTaGB	−0.511	LTbGB	−0.537	LTbGB	−0.537
LTbCI	0.493	LTbGreen	−0.510	LTbGGreen	−0.512	LTaGB	−0.511
LTbRB	−0.493	LTbBCI	0.498	LTaGB	−0.511	LTbGreen	−0.510
LTbRed	−0.487	LTbBRB	−0.498	LTbGreen	−0.510	LTbICI	0.499
LTbPCA1	−0.478	LTbCI	0.493	LTbCI	0.493	LTbIRB	−0.499
LTbSWIR1	−0.469	LTbRB	−0.493	LTbRB	−0.493	LTbIGreen	−0.493
LTbBlue	−0.453	LTbRed	−0.487	LTbRed	−0.487	LTbCI	0.493
LTaGreen	−0.450	LTbBGreen	−0.486	LTbGCI	0.483	LTbRB	−0.493
LTbS1B	−0.441	LTbPCA1	−0.478	LTbGRB	−0.483	LTbIRed	−0.488
LTaCI	0.431	LTbBRed	−0.476	LTbGRed	−0.480	LTbRed	−0.487
LTaRB	−0.431	LTbSWIR1	−0.469	LTbPCA1	−0.478	LTbPCA1	−0.478
LTbRG	−0.429	LTbBlue	−0.453	LTbSWIR1	−0.469	LTbSWIR1	−0.469
LTaPCA1	−0.419	LTaGreen	−0.450	LTaGCI	0.466	LTaICI	0.467

Nomenclature of the variable in Table 9: Remote sensing image (Abbreviation in Table 1) + Spectral index (Abbreviation in Table 2).

Table 10
Importance score (mean Z-score) between soil K_{ex} and relevant variables extracted from PAN and MS Landsat 8 images.

Multispectral image		MS and Brovey PAN images		MS and GS PAN images		MS and IHS PAN images	
Variable	MeanZ	Variable	MeanZ	Variable	MeanZ	Variable	MeanZ
LTaGB	10.54	LTbBGB	16.06	LTbGARVI	12.82	LTbIGB	12.63
LTbGB	9.69	LTbBRG	9.95	LTaGGB	11.72	LTaIGB	9.96
LTbRB	9.17	LTbBRB	7.73	LTbGGB	9.88	LTaIRB	9.05
LTbCI	9.05	LTbBCI	7.55	LTaGRB	9.39	LTaICI	8.90
LTaARVI	8.86	LTaGB	7.36	LTbGRG	9.38	LTaIGreen	8.26
LTbARVI	8.76	LTaRed	7.17	LTaGCI	9.19	LTaIRG	7.45
LTaRed	8.56	LTbGB	7.04	LTaGRG	8.34	LTaRed	6.77
LTbRG	8.50	LTbARVI	6.71	LTbGBlue	7.11	LTbCoastal	6.69
LTaRG	8.41	LTbCoastal	6.68	LTbGB	6.06	LTaIARVI	6.64
LTbCoastal	7.59	LTbPCA4	6.52	LTbT1	5.83	LTaIRed	6.55
LTaGreen	7.52	LTaGreen	6.32	LTbCoastal	5.83	LTaIBlue	6.23
LTbRed	7.43	LTaARVI	6.14	LTaGGreen	5.82	LTbARVI	6.08
LTaCI	7.16	LTbRB	6.13	LTaRed	5.77	LTbPCA4	6.03
LTaRB	7.15	LTbCI	5.94	LTbGRed	5.65	LTbGB	5.98
LTbGreen	7.07	LTaRG	5.83	LTbPCA4	5.63	LTbIRG	5.93
LTbSWIR1	6.83	LTbRG	5.82	LTaGB	5.57	LTaGreen	5.65
LTbT1	6.29	LTbRed	5.65	LTbT2	5.36	LTbICI	5.63
LTbBlue	6.12	LTbBlue	5.40	LTbARVI	5.34	LTbIRB	5.61
LTbT2	6.02	LTbPCA1	5.20	LTbPCA1	5.30	LTbBlue	5.32
LTbS1B	5.47	LTbGreen	4.88	LTaGreen	5.25	LTbRed	5.29
LTaBlue	5.10	LTbT1	4.68	LTbSWIR1	5.23	LTbRG	5.24
		LTaBlue	4.43	LTaGRed	5.05	LTbCI	5.14
				LTbGCI	5.04	LTaGB	5.13
				LTaGNIR	4.97	LTaARVI	5.12

Nomenclature of the variable in Table 10: Remote sensing image (Abbreviation in Table 1) + Spectral index (Abbreviation in Table 2).

band reflectances from PAN WorldView-2 images had relatively strong negative correlations with K_{ex}, and NIR-related spectral indices from PAN WorldView-2 images such as ARVI had relatively strong positive correlations ($R > 0.4$) with K_{ex}. ARVI, CI, GB, and RB of three PAN WorldView-2 images were all identified as relevant variables (Table 12). Spectral indices from new additional bands from WorldView-2 such as the ratio of NIR band 2 to red edge band (WVN2RE), NIR band 2 to red band (WVN2R), NIR band 2 to green band (WVN2G), and yellow band reflectance (WVYellow) were also identified as relevant variables with K_{ex} (Table 12).

3.4.3. Spatial characteristics of soil K_{ex} by different soil prediction models

Table 13 describes the eight soil K_{ex} prediction models based on the relevant spectral indices identified in Tables 10 and 12. Four maps in Fig. 8 demonstrated the similar spatial pattern of K_{ex}. K_{ex} prediction maps showed that the southwestern and northwestern areas of the village had relatively low K_{ex}, whereas the southeastern areas of the village had comparatively high K_{ex}. The prediction range (99.44–474.47 mg kg^{-1}) of K_{ex} map from model KLTG was wider than other maps. K_{ex} map by model KLTG (Fig. 8 (C)) had the most evident variation of K_{ex} among four maps. The spatial pattern of soil K_{ex} in Farmland A (Fig. 9) were shown to compare the differences between four soil K_{ex} prediction maps. Although K_{ex} maps by models KLTB (Fig. 9(B)) and KLTI (Fig. 9 (D)) had a spatial resolution of 15 m, their differences with K_{ex} map by model KLTM (Fig. 9(A)) was not evident from visual perspective. It suggests the incorporation of Brovey and IHS PAN Landsat 8 spectral indices into DSM may not remarkably increase the spatial quality of the soil K_{ex} map as did GS PAN spectral indices.

Four maps in Fig. 10 based on WorldView-2 and GeoEye-1 showed those maps can characterize complex and heterogeneous spatial pattern of K_{ex} in Kothapally. The K_{ex} maps in Farmland B by soil models based on MS and PAN spectral indices (Fig. 11(B)–(D)) had spatial resolution of 0.5 m and greatly enhanced the spatial characterization of K_{ex} compared with K_{ex} map by soil model based on MS spectral indices (Fig. 11(A)). Four maps in Fig. 11

Table 11
Linear correlations between soil K_{ex} and environmental variables extracted from PAN and MS WorldView-2 and GeoEye-1 images.

Multispectral image		MS and Brovey PAN images		MS and GS PAN images		MS and IHS PAN images	
Variable	R	Variable	R	Variable	R	Variable	R
WVPCA2	−0.496	WVBARVI	0.507	WVGARVI	0.505	WVIARVI	0.504
WVARVI	0.489	WVPCA2	−0.496	WVPCA2	−0.496	WVPCA2	−0.496
WVYellow	−0.477	WVBGreen	−0.493	WVARVI	0.489	WVARVI	0.489
WVRed	−0.471	WVARVI	0.489	WVYellow	−0.477	WVIGreen	−0.480
WVCI	0.467	WVBRed	−0.487	WVGRed	−0.475	WVIRed	−0.480
WVRB	−0.467	WVBBlue	−0.479	WVGCI	0.473	WVYellow	−0.477
WVGreen	−0.464	WVYellow	−0.477	WVGRB	−0.473	WVICI	0.475
WVBlue	−0.440	WVBCI	0.476	WVRed	−0.471	WVIRB	−0.475
WVN2R	0.429	WVBRB	−0.476	WVCI	0.467	WVRed	−0.471
WVRG	−0.423	WVRed	−0.471	WVRB	−0.467	WVCI	0.467
WVNDVIr	0.421	WVCI	0.467	WVGreen	−0.464	WVRB	−0.467
WVCIr	0.421	WVRB	−0.467	WVGGreen	−0.463	WVGreen	−0.464
WVN1RE	0.421	WVGreen	−0.464	WVGGB	−0.457	WVIGB	−0.459
WVN2RE	0.421	WVBRG	−0.458	WVGBlue	−0.447	WVIRG	−0.457
WVNDVI	0.418	WVBGB	−0.449	WVGRG	−0.446	WVIBlue	−0.449

Nomenclature of the variable in Table 11: Remote sensing image (Abbreviation in Table 1) + Spectral index (Abbreviation in Table 2).

Table 12
Importance score (mean Z-score) between soil K_{ex} and relevant variables extracted from PAN and MS WorldView-2 and GeoEye-1 images.

Multispectral image		MS and Brovey PAN images		MS and GS PAN images		MS and IHS PAN images	
Variable	MeanZ	Variable	MeanZ	Variable	MeanZ	Variable	MeanZ
GEARVI	13.22	GEARVI	11.21	GEARVI	11.76	GEARVI	11.55
GEGreen	9.45	GEBGB	8.63	WVGARVI	8.84	GEIGB	10.78
WVARVI	7.43	WVBARVI	8.48	WVPCA2	8.76	WVPCA2	8.42
WVN2RE	7.17	WVPCA2	8.27	WVGGB	7.18	WVIARVI	8.22
WVRed	6.95	GEGreen	6.89	GEGreen	6.72	WVIGB	8.00
WVN2R	6.63	WVBGreen	6.29	WVN2RE	5.68	WVIGreen	6.66
WVYellow	6.51	WVBGB	6.20	WVARVI	5.67	GEGreen	6.37
WVGB	6.14	WVBRed	5.74	WVN2G	5.40	WVN2RE	6.04
WVN2G	6.05	WVN2RE	5.69	WVN2R	5.26	WVIRB	5.68
WVREG	5.18	WVBRB	5.48	WVREG	5.16	WVN2R	5.53
		WVBCI	5.45	WVGRB	4.98	WVICI	5.50
		WVARVI	5.36	WVGCI	4.97	WVARVI	5.47
		WVN2R	5.04	WVN2B	4.93	WVIRed	5.26
				WVCoastal	4.89	WVN2G	5.18
						WVREG	5.01

Nomenclature of the variable in Table 12: Remote sensing image (Abbreviation in Table 1) + Spectral index (Abbreviation in Table 2).

Table 13
Validation results of different soil K_{ex} models.

Models	Adj R^2	RMSE (mg kg^{-1})	RPD	RPIQ	Spectral library	Grid size (m)
KLTM	0.51	79.73	1.39	1.91	17 spectral indices from MS Landsat 8 images in Table 10	30
KLTB	0.52	78.25	1.42	1.95	17 spectral indices from MS and Brovey PAN Landsat 8 images in Table 10	15
KLTG	0.58	76.52	1.45	1.99	17 spectral indices from MS and GS PAN Landsat 8 images in Table 10	15
KLTI	0.55	77.25	1.44	1.97	17 spectral indices from MS and IHS PAN Landsat 8 images in Table 10	15
KWGM	0.46	83.83	1.32	1.82	10 spectral indices from MS WorldView-2 and GeoEye-1 images in Table 12	2
KWGB	0.50	81.26	1.37	1.88	15 spectral indices from MS and Brovey PAN WorldView-2 and GeoEye-1 images in Table 12	0.5
KWGG	0.52	82.08	1.35	1.86	15 spectral indices from MS and GS PAN WorldView-2 and GeoEye-1 images in Table 12	0.5
KWGI	0.51	81.09	1.37	1.88	14 spectral indices from MS and IHS PAN WorldView-2 and GeoEye-1 images in Table 12	0.5

Nomenclature of model name in Table 13: Soil property + Remote sensing image + Image type.
Soil property: K, exchangeable potassium; Remote sensing image: LT, Landsat 8 images; WG, WorldView-2 and GeoEye-1 images. Image Type: M, multispectral image, B, Brovey image, G, GS image, I, IHS image.

can clearly characterize the lower K_{ex} in bare soil field block and road, and relatively higher K_{ex} in the vegetated field block.

3.4.4. Assessment of soil K_{ex} prediction models

Table 13 compares validation results of eight soil K_{ex} prediction models. Comparing Landsat 8-based soil K_{ex} prediction models, the model fit is ordered by KLTG > KLTI > KLTB > KLTM, and the prediction error is ordered by KLTM > KLTB > KLTI > KLTG. Comparing WorldView-2/GeoEye-1-based soil K_{ex} prediction models, the model fit is ordered by KWGG > KWGI > KWGB > KWGM, and the prediction error is ordered by KWGM > KWGG > KWGB > KWGI. Model KLTG based on MS and GS PAN Landsat 8 spectral indices can attain the highest model fit (R^2 = 0.58) and lowest prediction error (RMSE = 76.52 mg kg^{-1}) among all the models.

4. Discussion

4.1. Remote sensing-based Digital Soil Mapping in smallholder farm settings

Digital soil mapping (DSM) has been applied in undernourished smallholder farm settings in semi-arid regions such as Africa and

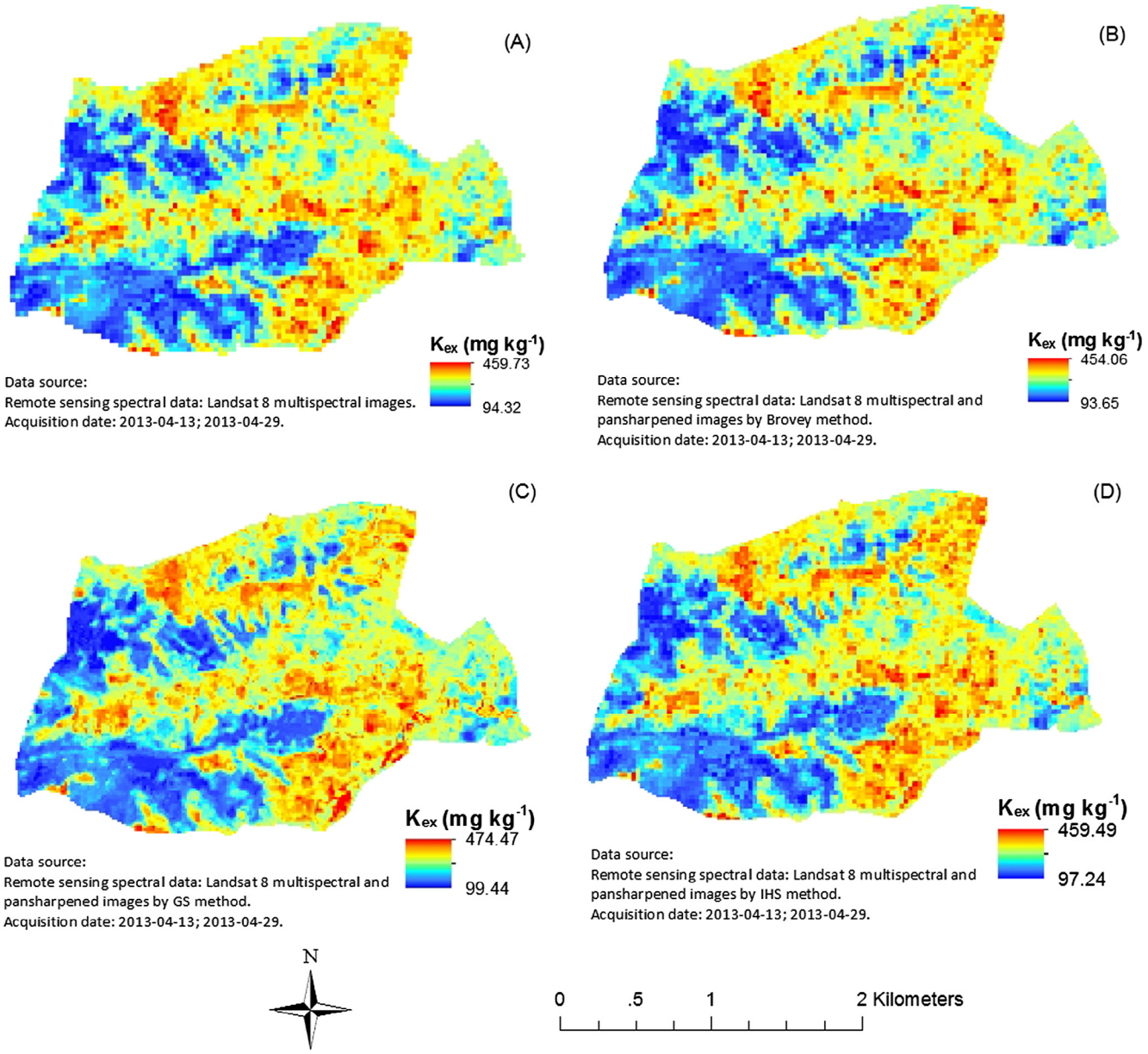

Fig. 8. Soil K_{ex} prediction at 0–15 cm depth in Kothapally by (A) model KLTM, (B) model KLTB, (C) model KLTG, (D) model KLTI.

India. Kuriakose et al. (2009) compared ordinary kriging, regression kriging, and stochastic simulation methods to predict soil depth in South India. Ordinary kriging was employed to create spatial distribution maps of total and extractable zinc in cultivated acid soils situated in four Indian States (Behera et al., 2011). Most previous DSM research in smallholder farm settings did not include environmental variables such as remote sensing data in their models. Most DSM research not only utilizes the continuous remote sensing spectral information, but also categorical environmental variables (Wiesmeier et al., 2011). However, categorical environmental variables such as precipitation, soil depth, soil types, land use, and ecological regions are not easy to obtain in small-scale farm settings due to the shortage of historical data. Without categorical covariates and soil laboratory spectral data, the soil prediction models in this research only utilizing remote sensing spectral indices can still attain fair prediction accuracies for TN and K_{ex}.

Machine learning and data reduction techniques can help select the best performing parsimonious soil prediction models (Xiong et al., 2014). The relevant variable searching method (Boruta Algorithm) can greatly reduce the multi-collinearity of the spectral indices, and some spectral indices that had relatively weak linear correlations with TN and K_{ex} were also identified as relevant variables. The spectral indices of different images identified as relevant variables with soil nutrients (TN and K_{ex}) were diverse. The VIS-NIR-related spectral indices can reflect land surface vegetation. The strong positive linear relationships between soil nutrients (TN and K_{ex}) and VIS-NIR-related spectral indices such as ARVI and NDVI indicated the vegetated areas were prone to contain higher soil nutrients. Crust Index (CI) incorporating red and blue band reflectance also had strong positive correlations with soil TN and K_{ex}. Soil crust can prevent soil erosion and is prone to contain more silt and clay materials due to the adhesive properties of microphytes (Danin, 1991). Biological soil crusts can greatly affect

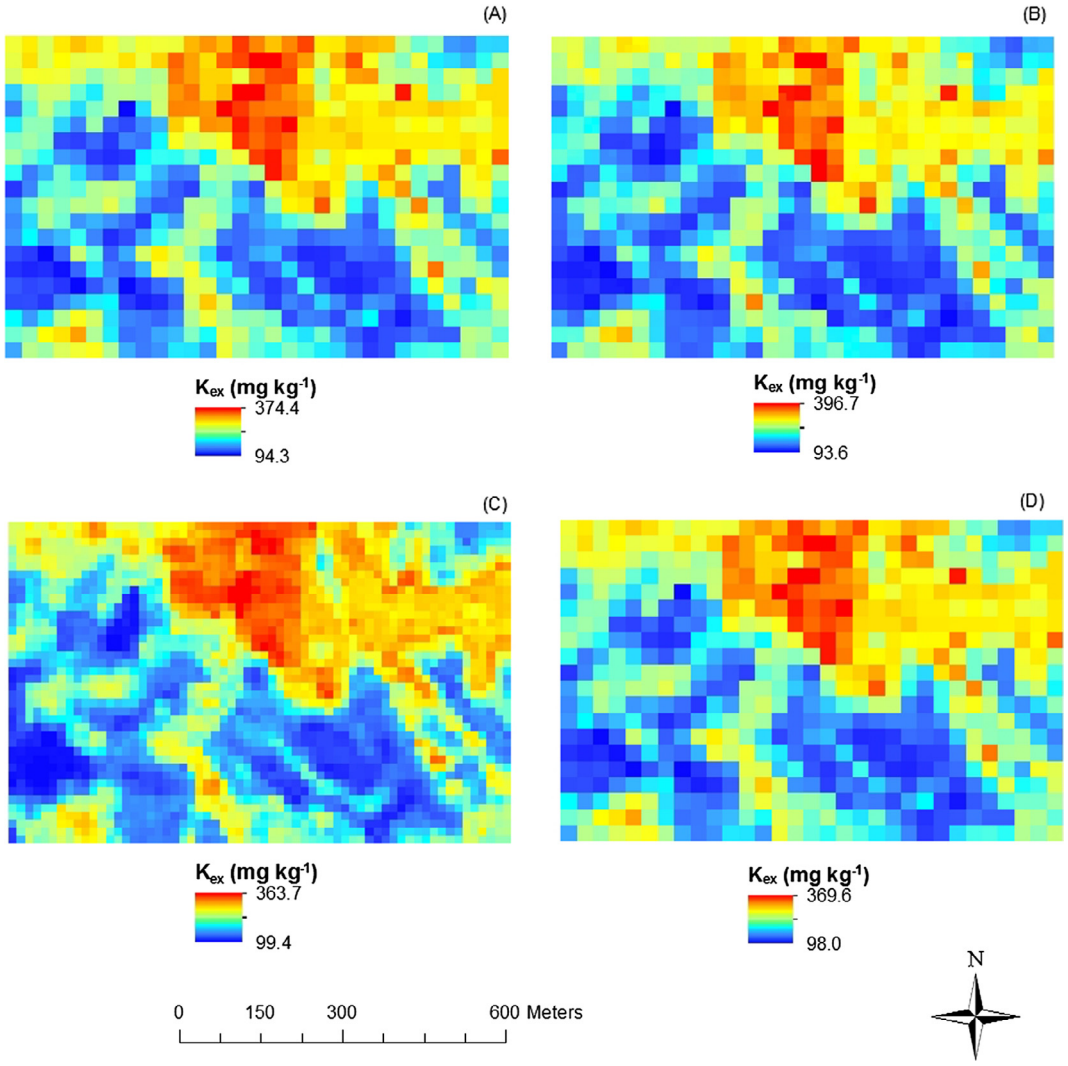

Fig. 9. Soil K_{ex} prediction at 0–15 cm depth in Farmland A of Kothapally by (A) model KLTM, (B) model KLTB, (C) model KLTG, (D) model KLTI.

the nitrogen cycle of semi-arid ecosystems, as some of the organisms forming them are able to fix atmospheric nitrogen (Castillo-Monroy et al., 2010).

SWIR is sensitive to the variation of water, leafy vegetation, and soil moisture. There is strong absorption by water in green leaves and wet soils in SWIR spectrum region. Soils have broad and shallow absorption features related to soil organic matter at wavelength between 400 and 2500 nm, and the reflectance of soil decreases as organic matter increases (Ustin et al., 2004). Weidong et al. (2002) also demonstrated soil surface reflectance was prone to decrease when the soil moisture increases. The strong negative correlations between soil nutrients (TN and K_{ex}) and surface reflectances of Vis-NIR and SWIR bands indicated the soils with more organic carbon and water contents were also prone to contain more soil TN and K_{ex} in the study area. Many researchers also have utilized TIR-related indices to estimate soil moisture, soil temperature, drought, and plant water stress (Karnieli et al., 2010; Pons-Fernández et al., 2004). This research suggested that at-satellite brightness temperatures (T1 and T2) from Landsat 8 images are important environmental variables that can reflect the soil nutrient status in semi-arid farmland. Some new spectral indices extracted from coastal, yellow, red edge and near infrared band 2 from WorldView-2 were identified as relevant variables with TN and K_{ex}, and were not filtered out by Boruta algorithm. Red edge-related spectral models were widely utilized to predict plant chlorophyll and nitrogen content in many research (Cho and Skidmore, 2006; Clevers and Gitelson, 2013). This research suggested the spectral information of these new bands from commercial satellite images including red edge band can provide valuable information to predict soil nutrients in the study area. Overall, a positive feedback between soil nutrients (TN and K_{ex}) and soil moisture, vegetation, and soil crusts may exist in the study area.

Soil TN and K_{ex} in the central strip area of the village was relatively high. From previous crop survey, crops were planted in both rainy and dry season in the central trip of the village from west to east. The plant biomass input from the crops into the soil may lead to more organic carbon and soil nutrients in this area. Vertisols in South India tend to contain large amounts of potassium (Dhillon and Dhillon, 1991). Only small areas in the southeastern area of the village had K_{ex} smaller than 150 mg kg^{-1}, which can be defined as low level according to the classification from Horneck et al. (2011). Southwestern area of the village had relatively low TN and K_{ex}, where cotton was only planted in the rainy season and became fallow land in the dry season. The long term cultivation and limited fertilizer and manure input may account for the low soil TN and K_{ex} in the southwestern area of the village.

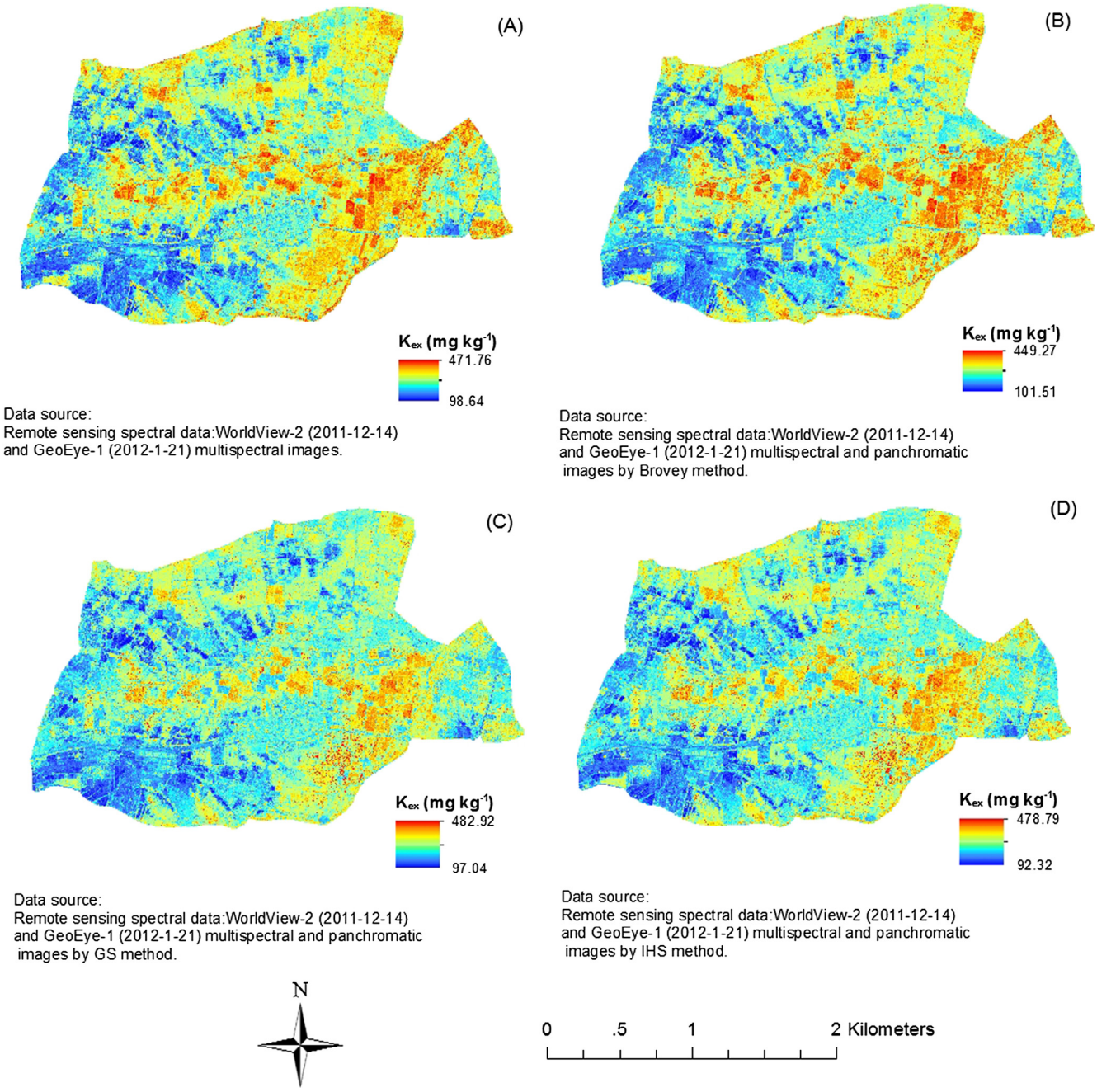

Fig. 10. Soil K_{ex} prediction at 0–15 cm depth in Kothapally by (A) model KWGM, (B) model KWGB, (C) model KWGG, (D) model KWGI.

4.2. Effect of different image pan-sharpening methods on soil prediction models

Some identical spectral indices such as ARVI, CI, and ratio of visible bands from both the PAN and MS images had relatively strong correlations and were identified as relevant variables with TN and K_{ex}. Our research emphasizes image pan-sharpening techniques not only improve the spatial resolution, but also retain the spectral fidelity of multispectral images (Zhang, 2010) since the spectral characteristics of MS and PAN spectral data were similar. With the incorporation of PAN spectral indices, more spectral indices were identified as relevant variables with soil TN and K_{ex}. Some PAN spectral indices had stronger linear correlations and higher importance scores with soil properties than all the MS spectral indices. From model validation, all models based on PAN and MS image spectral indices showed higher prediction capabilities and more detailed characterization of soil properties compared with the models only based on MS image spectral indices.

Although the Brovey method is mathematically simple and easy to implement, it normalizes the spectral information of MS image at the spatial resolution of the panchromatic images, and tends to smooth the spectral information. The reduction of spectral information in the Brovey PAN image was mainly caused by the mismatch of spectral range and pixel values between the panchromatic and multispectral bands (Tu et al., 2004). The different pixel values of the panchromatic and multispectral bands lead to the fusion of panchromatic band information into the multispectral bands information in Brovey method. In this research, the spatial quality of Brovey PAN images were not as good as the GS PAN images.

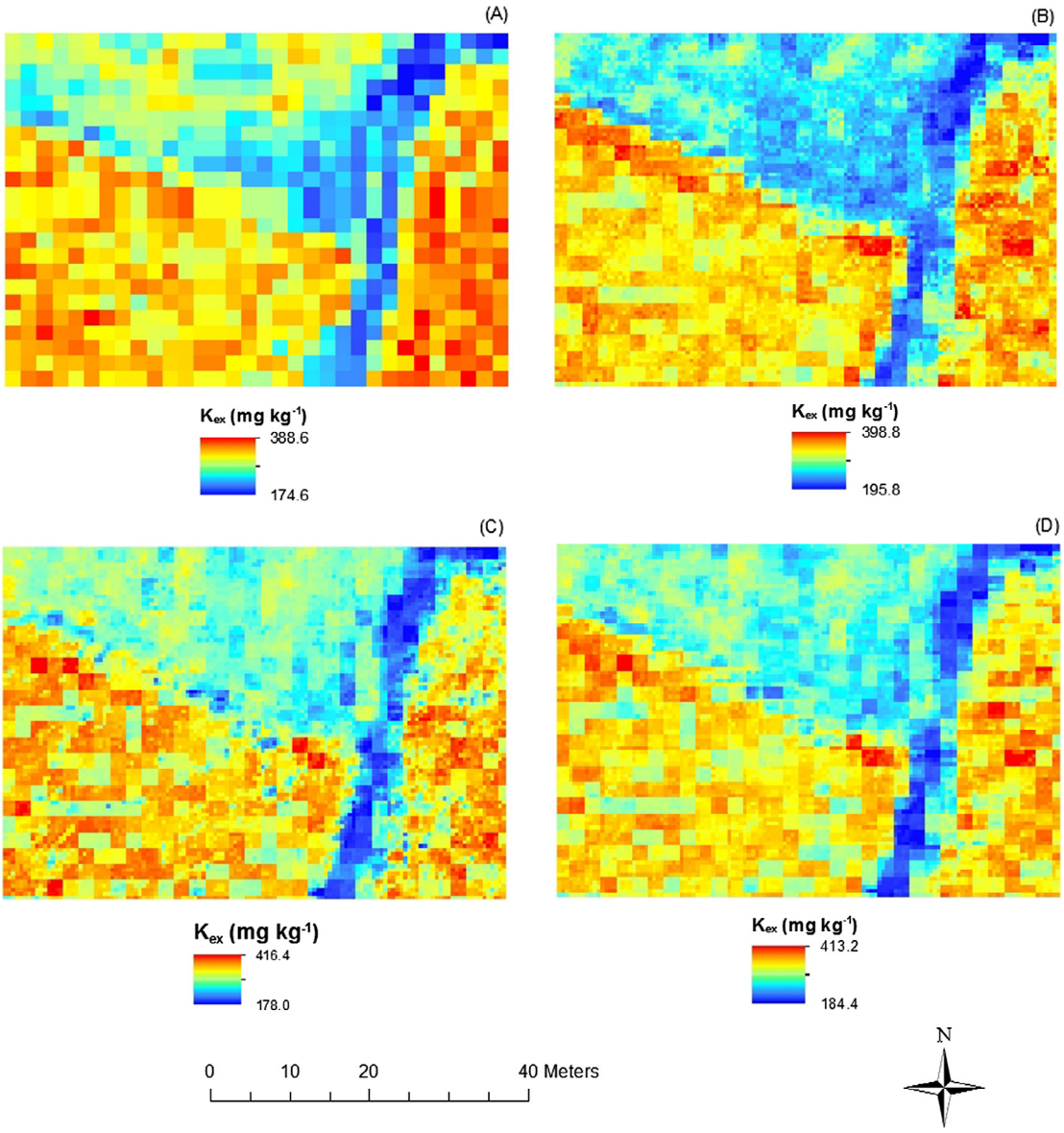

Fig. 11. Soil K_{ex} prediction at 0–15 cm depth in Farmland B by (A) model KWGM, (B) model KWGB, (C) model KWGG, (D) model KWGI.

The spectral information of the IHS space is largely determined by hue and saturation (Al-Wassai et al., 2011). By comparing four pan-sharpening methods, Johnson (2014) indicated that IHS PAN vegetation indices were more similar to the finer spatial resolution reference vegetation indices data compared with Brovey, Additive Wavelet Transform, and Smoothing Filter-based Intensity Modulation PAN vegetation indices images.

Most research proved that the GS PAN images preserve the spectral and spatial information of the ground features in the original images better than the Brovey and IHS methods (Aiazzi et al., 2007; Sarp, 2014; Zhang and Huang, 2015). The GS method is a more computationally complex method though. Li et al. (2004) generalized two advantages of the GS method: (1) the number of bands in the Gram-Schmidt vector orthogonalization is not limited and (2) the spectral characteristics of the lower spatial resolution multispectral data are preserved in the form of a simulated low resolution panchromatic band. GS PAN images significantly enhanced the structural and textural details of the previous MS images. The variations of crop, residues, and soil in the small farmland were more pronounced and clearly embodied by the GS PAN images than by other PAN images. The research also suggested the soil maps based on GS PAN spectral indices showed more evident spatial variation compared with soil maps based on other PAN spectral indices.

However, no single pan-sharpening method can be considered as "best" for all the soil prediction models. From Tables 8 and 13, it is noticed that the prediction errors and model fit of PAN/MS spectral indices-based soil prediction models did not demonstrate significant difference. The best pan-sharpening method depends on the task (visualization, biomass mapping, soil mapping, image classification) and on size and time constraints (speed, complexity) (Johnson et al., 2014). By comparing the prediction accuracy of different models, there is no specific pan-sharpened spectral indices that always had the strongest prediction capability with soil TN and K_{ex}.

4.3. Significance of pan-sharpened spectral data on soil prediction models

In this research, we utilized and examined the image pan-sharpening technique and pan-sharpened spectral data in DSM. Although soil prediction models based on Landsat 8 can attain rel-

atively fair prediction accuracy for TN and $K_{ex,}$ the coarse spatial resolution of Landsat 8 is still problematic that hinders the widely application of Landsat 8 in DSM in smallholder farm settings. Image pan-sharpening technique resolves this bottleneck and increases the spatial resolution of soil prediction maps based on Landsat 8. Those soil maps based on MS and PAN Landsat 8 images has a significant value of practical application in large scale research due to its free and convenient image acquisition. Digital soil prediction models especially those utilizing WorldView-2 and GeoEye-1 images have the high capability to capture and monitor the variation of soil nutrient status in semi-arid smallholder farm settings. MS and PAN WorldView-2/GeoEye-1-based soil prediction maps enhance the subtle depiction of soil property variation to 0.5 m grid size in this study. However, the WorldView-2/GeoEye-1-based soil prediction models did not necessarily had higher prediction accuracy compared with Landsat-based soil prediction models.

Agricultural extension workers, scientists, smallholder farmers and other stakeholders can utilize those remote sensing-based soil maps to help identify the variation of soil nutrients in a specific smallholder village, and implement field-specific soil management schemes. The image pan-sharpening technique can also enhance the capability to identify ground features. For example, while the roads were barely visible in MS Landsat 8 image (Fig. 3(A)), they were easily identified in PAN Landsat 8 images (Fig. 3(B)–(D)). MS and PAN WorldView-2 and GeoEye-1 images can identify road, crop types, irrigation facilities and residential areas, and those information is valuable to the land use management, water resource management and plant protection.

5. Conclusions

PAN remote sensing spectral indices have similar spectral characteristics with soil TN and K_{ex} as MS remote sensing spectral indices. Soil TN and K_{ex} prediction models based on MS and PAN Landsat 8 spectral indices all have higher prediction accuracy and finer spatial resolution compared with those only based on MS Landsat 8 spectral indices. In addition, soil TN and K_{ex} prediction models based on MS and PAN WorldView-2, and GeoEye-1 spectral indices all have higher prediction accuracy and finer spatial resolution compared with those only based on MS WorldView-2, and GeoEye-1 spectral indices. There is no soil prediction model incorporating the specific type of pan-sharpened spectral indices that always had the strongest prediction capability with soil TN and K_{ex}. In all, the image pan-sharpening technique (1) preserves the spectral behavior of the MS image; (2) improves the spatial resolution of the soil prediction map; (3) increases the model performance of soil prediction models; (4) enhances the structural and textural details of ground feature; (5) help policy makers establish agricultural and soil management policies in smallholder farm settings; (6) requires no new image purchasing and (7) have high potential to apply to the Digital Soil Mapping research in smallholder farm settings all over the world.

Acknowledgements

This project used resources provided by the grant award No. 1201943 "Development of a Geospatial Soil-Crop Inference Engine for Smallholder Farmers" EAGER National Science Foundation. The soil analysis was performed in the soil laboratory at the International Crops Research Institute for the Semi-Arid Tropics (ICRISAT) in Patancheru/Hyderabad, India. We thank Christopher M. Clingensmith at University of Florida, and other ICRISAT staff members and villagers of Kothapally for support with field sampling. We also thank Yiming Xu's PhD committee members Dr. Thomas K. Frazer and Dr. Vimala D. Nair for their commitment and guidance. A matching assistantship for Yiming Xu was provided by School of Natural Resources and Environment, University of Florida, and China Scholarship Council.

References

Aiazzi, B., Baronti, S., Selva, M., 2007. Improving component substitution pansharpening through multivariate regression of MS +pan data. IEEE Trans. Geosci. Remote Sens. 45, 3230–3239. http://dx.doi.org/10.1109/TGRS.2007.901007.

Alparone, L., Aiazzi, B., Baronti, S., Garzelli, A., 2015. Remote Sensing Image Fusion. CRC Press.

Al-Wassai, F.A., Kalyankar, N., Al-Zuky, A.A., 2011. The IHS Transformations Based Image Fusion. arXiv preprint arXiv:1107.4396.

Behera, S.K., Singh, M.V., Singh, K.N., Todwal, S., 2011. Distribution variability of total and extractable zinc in cultivated acid soils of India and their relationship with some selected soil properties. Geoderma 162, 242–250. http://dx.doi.org/10.1016/j.geoderma.2011.01.016.

Bhattacharyya, R., Prakash, V., Kundu, S., Ghosh, B.N., Srivastva, A.K., Gupta, H.S., 2006. Potassium balance as influenced by farmyard manure application under continuous soybean–wheat cropping system in a Typic Haplaquept. Geoderma 137, 155–160. http://dx.doi.org/10.1016/j.geoderma.2006.08.006.

Breiman, L., 2001. Random forests. Mach. Learn. 45, 5–32. http://dx.doi.org/10.1023/A:1010933404324.

Castillo-Monroy, A.P., Maestre, F.T., Delgado-Baquerizo, M., Gallardo, A., 2010. Biological soil crusts modulate nitrogen availability in semi-arid ecosystems: insights from a Mediterranean grassland. Plant Soil 333, 21–34. http://dx.doi.org/10.1007/s11104-009-0276-7.

Chander, G., Wani, S.P., Sahrawat, K.L., Dixit, S., Venkateswarlu, B., Rajesh, C., Rao, P. N., Pardhasaradhi, G., 2014. Soil test-based nutrient balancing improved crop productivity and rural livelihoods: case study from rainfed semi-arid tropics in Andhra Pradesh, India. Arch. Agron. Soil Sci. 60, 1051–1066. http://dx.doi.org/10.1080/03650340.2013.871706.

Cho, M.A., Skidmore, A.K., 2006. A new technique for extracting the red edge position from hyperspectral data: the linear extrapolation method. Remote Sens. Environ. 101, 181–193. http://dx.doi.org/10.1016/j.rse.2005.12.011.

Clevers, J.G.P.W., Gitelson, A.A., 2013. Remote estimation of crop and grass chlorophyll and nitrogen content using red-edge bands on Sentinel-2 and -3. Int. J. Appl. Earth Obs. Geoinf. 23, 344–351. http://dx.doi.org/10.1016/j.jag.2012.10.008.

Cohen, W.B., 1991. Response of vegetation indices to changes in three measures of leaf water stress. Photogram. Eng. Remote Sens., 195–202

Danin, A., 1991. Plant adaptations in desert dunes. J. Arid Environ. 21, 193–212.

Daughtry, C.S.T., Walthall, C.L., Kim, M.S., de Colstoun, E.B., McMurtrey III, J.E., 2000. Estimating corn leaf chlorophyll concentration from leaf and canopy reflectance. Remote Sens. Environ. 74, 229–239. http://dx.doi.org/10.1016/S0034-4257(00)00113-9.

Dhillon, S.K., Dhillon, K.S., 1991. Characterisation of potassium in red (alfisols), black (vertisols) and alluvial (inceptisols and entisols) soils of India using electro-ultrafiltration. Geoderma 50, 185–196. http://dx.doi.org/10.1016/0016-7061(91)90033-P.

Ehlers, M., Klonus, S., Johan Åstrand, P., Rosso, P., 2010. Multi-sensor image fusion for pansharpening in remote sensing. Int. J. Image Data Fusion 1, 25–45. http://dx.doi.org/10.1080/19479830903561985.

Francés, A.P., Lubczynski, M.W., 2011. Topsoil thickness prediction at the catchment scale by integration of invasive sampling, surface geophysics, remote sensing and statistical modeling. J. Hydrol. 405, 31–47. http://dx.doi.org/10.1016/j.jhydrol.2011.05.006.

Gao, B., 1996. NDWI—A normalized difference water index for remote sensing of vegetation liquid water from space. Remote Sens. Environ. 58, 257–266. http://dx.doi.org/10.1016/S0034-4257(96)00067-3.

Gitelson, A.A., Kaufman, Y.J., Merzlyak, M.N., 1996. Use of a green channel in remote sensing of global vegetation from EOS-MODIS. Remote Sens. Environ. 58, 289–298. http://dx.doi.org/10.1016/S0034-4257(96)00072-7.

Gitelson, A.A., Viña, A., Ciganda, V., Rundquist, D.C., Arkebauer, T.J., 2005. Remote estimation of canopy chlorophyll content in crops. Geophys. Res. Lett. 32, L08403. http://dx.doi.org/10.1029/2005GL022688.

Gitelson, A., Merzlyak, M.N., 1994. Spectral reflectance changes associated with autumn senescence of aesculus hippocastanum L. and Acer platanoides L. Leaves. Spectral features and relation to chlorophyll estimation. J. Plant Physiol. 143, 286–292. http://dx.doi.org/10.1016/S0176-1617(11)81633-0.

Haboudane, D., Miller, J.R., Tremblay, N., Zarco-Tejada, P.J., Dextraze, L., 2002. Integrated narrow-band vegetation indices for prediction of crop chlorophyll content for application to precision agriculture. Remote Sens. Environ. 81, 416–426. http://dx.doi.org/10.1016/S0034-4257(02)00018-4.

Heung, B., Bulmer, C.E., Schmidt, M.G., 2014. Predictive soil parent material mapping at a regional-scale: a Random Forest approach. Geoderma 214–215, 141–154. http://dx.doi.org/10.1016/j.geoderma.2013.09.016.

Hitziger, M., Ließ, Mareike, 2014. Comparison of three supervised learning methods for digital soil mapping: application to a complex terrain in the ecuadorian andes. Appl. Environ. Soil Sci., e809495 http://dx.doi.org/10.1155/2014/809495.

Horneck, D.A., Sullivan, D.M., Owen, J.S., Hart, J.M., 2011. Soil test interpretation guide. [Corvallis, Or.]: Oregon State University, Extension Service.

Jalan, S., Sokhi, B.S., 2012. Comparison of different pan-sharpening methods for spectral characteristic preservation: multi-temporal CARTOSAT-1 and IRS-P6 LISS-IV imagery. Int. J. Remote Sens. 33, 5629–5643. http://dx.doi.org/10.1080/01431161.2012.666811.

Johnson, B., 2014. Effects of pansharpening on vegetation indices. ISPRS Int. J. Geo-Inform. 3, 507–522.

Johnson, B.A., Scheyvens, H., Shivakoti, B.R., 2014. An ensemble pansharpening approach for finer-scale mapping of sugarcane with Landsat 8 imagery. Int. J. Appl. Earth Obs. Geoinf. 33, 218–225. http://dx.doi.org/10.1016/j.jag.2014.06.003.

Kalpoma, K.A., Kudoh, J.-I., 2007. Image fusion processing for IKONOS 1-m color imagery. IEEE Trans. Geosci. Remote Sens. 45, 3075–3086. http://dx.doi.org/10.1109/TGRS.2007.897692.

Karathanassi, V., Kolokousis, P., Ioannidou, S., 2007. A comparison study on fusion methods using evaluation indicators. Int. J. Remote Sens. 28, 2309–2341. http://dx.doi.org/10.1080/01431160600606890.

Karnieli, A., 1997. Development and implementation of spectral crust index over dune sands. Int. J. Remote Sens. 18, 1207–1220. http://dx.doi.org/10.1080/014311697218368.

Karnieli, A., Agam, N., Pinker, R.T., Anderson, M., Imhoff, M.L., Gutman, G.G., Panov, N., Goldberg, A., 2010. Use of NDVI and land surface temperature for drought assessment: merits and limitations. J. Clim. 23, 618–633. http://dx.doi.org/10.1175/2009JCLI2900.1.

Kaufman, Y.J., Tanré, D., 1996. Strategy for direct and indirect methods for correcting the aerosol effect on remote sensing: From AVHRR to EOS-MODIS. Remote Sens. Environ. 55, 65–79. http://dx.doi.org/10.1016/0034-4257(95)00193-X.

Krom, M.D., 1980. Spectrophotometric determination of ammonia: a study of a modified Berthelot reaction using salicylate and dichloroisocyanurate. Analyst 105, 305–316. http://dx.doi.org/10.1039/AN9800500305.

Kuriakose, S.L., Devkota, S., Rossiter, D.G., Jetten, V.G., 2009. Prediction of soil depth using environmental variables in an anthropogenic landscape, a case study in the Western Ghats of Kerala, India. CATENA 79, 27–38. http://dx.doi.org/10.1016/j.catena.2009.05.005.

Laben, C.A., Brower, B.V., 2000. Process for Enhancing the Spatial Resolution of Multispectral Imagery using Pan-sharpening. US6011875 A.

Li, C., Liu, L., Wang, J., Zhao, C., Wang, R., 2004. Comparison of two methods of the fusion of remote sensing images with fidelity of spectral information. Geoscience and Remote Sensing Symposium, 2004. IGARSS '04. Proceedings. 2004 IEEE International. Presented at the Geoscience and Remote Sensing Symposium, 2004. IGARSS '04. Proceedings. 2004 IEEE International, vol. 4, pp. 2561–2564. http://dx.doi.org/10.1109/IGARSS.2004.1369819.

Liaw, A., Wiener, M., 2002. Classification and regression by randomForest. R News 2, 18–22.

Lopatin, J., Dolos, K., Hernández, H.J., Galleguillos, M., Fassnacht, F.E., 2016. Comparing Generalized Linear Models and random forest to model vascular plant species richness using LiDAR data in a natural forest in central Chile. Remote Sens. Environ. 173, 200–210. http://dx.doi.org/10.1016/j.rse.2015.11.029.

Marshall, M., Thenkabail, P., 2015. Advantage of hyperspectral EO-1 Hyperion over multispectral IKONOS, GeoEye-1, WorldView-2, Landsat ETM+, and MODIS vegetation indices in crop biomass estimation. ISPRS J. Photogram. Remote Sens. 108, 205–218. http://dx.doi.org/10.1016/j.isprsjprs.2015.08.001.

McBratney, A.B., Mendonça Santos, M.L., Minasny, B., 2003. On digital soil mapping. Geoderma 117, 3–52. http://dx.doi.org/10.1016/S0016-7061(03)00223-4.

Musick, H.B., Pelletier, R.E., 1988. Response to soil moisture of spectral indexes derived from bidirectional reflectance in thematic mapper wavebands. Remote Sens. Environ. 25, 167–184. http://dx.doi.org/10.1016/0034-4257(88)90099-5.

Nellis, M.D., Briggs, J.M., 1992. Transformed vegetation index for measuring spatial variation in drought impacted biomass on Konza Prairie, Kansas. Transact. Kansas Acad. Sci. 95 (1903), 93–99. http://dx.doi.org/10.2307/3628024.

Pons-Fernández, X., Cuadrat-Prats, J., Vicente-Serrano, S., 2004. Mapping soil moisture in the central Ebro river valley (northeast Spain) with Landsat and NOAA satellite imagery: a comparison with meteorological data. Int. J. Remote Sens., 4325–4350

Qi, J., Chehbouni, A., Huete, A.R., Kerr, Y.H., Sorooshian, S., 1994. A modified soil adjusted vegetation index. Remote Sens. Environ. 48, 119–126. http://dx.doi.org/10.1016/0034-4257(94)90134-1.

Rikimaru, A., Miyatake, S., 1997. Development of forest canopy density mapping and monitoring model using indices of vegetation, bare soil and shadow. Available at <http://www.gisdevelopment.net/aars/acrs/1997/ts5/index.shtmm>.

Rock, B.N., Vogelmann, J.E., Williams, D.L., Vogelmann, A.F., Hoshizaki, T., 1986. Remote detection of forest damage. Bioscience 36, 439–445. http://dx.doi.org/10.2307/1310339.

Rogers, A.S., Kearney, M.S., 2004. Reducing signature variability in unmixing coastal marsh Thematic Mapper scenes using spectral indices. Int. J. Remote Sens. 25, 2317–2335. http://dx.doi.org/10.1080/01431160310001618103.

Rouse, J.W., Haas, R.H., Schell, J.A., Deering, D.W., 1974. Monitoring vegetation systems in the great plains with erts. NASA Spec. Publ. 351, 309.

Rudnicki, W., Kursa, M., 2010. Feature selection with the boruta package. J. Stat. Softw. 36, 1–13.

Sahrawat, K.L., Wani, S.P., Pardhasaradhi, G., Murthy, K.V.S., 2010. Diagnosis of secondary and micronutrient deficiencies and their management in rainfed agroecosystems: case study from Indian semi-arid tropics. Commun. Soil Sci. Plant Anal. 41, 346–360. http://dx.doi.org/10.1080/00103620903462340.

Sarp, G., 2014. Spectral and spatial quality analysis of pan-sharpening algorithms: a case study in Istanbul. Europ. J. Remote Sens. 47, 19–28.

Sims, D.A., Gamon, J.A., 2002. Relationships between leaf pigment content and spectral reflectance across a wide range of species, leaf structures and developmental stages. Remote Sens. Environ. 81, 337–354. http://dx.doi.org/10.1016/S0034-4257(02)00010-X.

Sreedevi, T., Shiferaw, B., Wani, S., 2004. Adarsha Watershed in Kothapally Understanding the Drivers of Higher Impact: Global Theme on Agroecosystems Report no. 10.

Srinivasarao, C., Kundu, S., Ramachandrappa, B.K., Reddy, S., Lal, R., Venkateswarlu, B., Sahrawat, K.L., Naik, R.P., 2013a. Potassium release characteristics, potassium balance, and fingermillet (Eleusine coracana G.) yield sustainability in a 27-year long experiment on an Alfisol in the semi-arid tropical India. Plant Soil 374, 315–330. http://dx.doi.org/10.1007/s11104-013-1877-8.

Srinivasarao, C., Venkateswarlu, B., Lal, R., Singh, A.K., Kundu, S., 2013b. Chapter five - sustainable management of soils of dryland ecosystems of india for enhancing agronomic productivity and sequestering carbon. In: Sparks, D.L. (Ed.), Advances in Agronomy. Academic Press, pp. 253–329.

Thomas, G.W., 1982. Exchangeable cations. Methods of soil analysis. Part 2. Chemical and microbiological properties, pp. 159–165.

Tu, T.-M., Huang, P.S., Hung, C.-L., Chang, C.-P., 2004. A fast intensity-hue-saturation fusion technique with spectral adjustment for IKONOS imagery. IEEE Geosci. Remote Sens. Lett. 1, 309–312. http://dx.doi.org/10.1109/LGRS.2004.834804.

Tu, T.-M., Su, S.-C., Shyu, H.-C., Huang, P.S., 2001. Efficient intensity-hue-saturation-based image fusion with saturation compensation. Opt. Eng. 40, 720–728. http://dx.doi.org/10.1117/1.1355956.

Ustin, S.L., Roberts, D.A., Gamon, J.A., Asner, G.P., Green, R.O., 2004. Using imaging spectroscopy to study ecosystem processes and properties. Bioscience 54, 523–534. http://dx.doi.org/10.1641/0006-3568(2004) 054[0523:UISTSE]2.0.CO;2.

Van, G.J., Pohl, C., 1994. Image fusion: issues, techniques and applications. Intelligent image fusion. Presented at the Proceedings EARSeL Workshop, Strasbourg, France, edited by Genderen JL Van, Cappellini V, pp. 20–59.

Vaudour, E., Bel, L., Gilliot, J.M., Coquet, Y., Hadjar, D., Cambier, P., Michelin, J., Houot, S., 2013. Potential of SPOT multispectral satellite images for mapping topsoil organic carbon content over peri-urban Croplands. Soil Sci. Soc. Am. J. 77, 2122. http://dx.doi.org/10.2136/sssaj2013.02.0062.

Wang, J., Ling, Z., Wang, Y., Zeng, H., 2016. Improving spatial representation of soil moisture by integration of microwave observations and the temperature–vegetation–drought index derived from MODIS products. ISPRS J. Photogram. Remote Sens. 113, 144–154. http://dx.doi.org/10.1016/j.isprsjprs.2016.01.009.

Wang, J., Tsang, W.W., Marsaglia, G., 2003. Evaluating Kolmogorov's distribution. J. Stat. Softw. 8.

Wani, S., Singh, H., Sreedevi, T., Pathak, P., Rego, T., Shiferaw, B., Iyer, S.R., 2003. Farmer-participatory integrated watershed management: adarsha watershed, Kothapally India-an innovative and upscalable approach. J. SAT Agricult. Res. 2, 1–27.

Weidong, L., Baret, F., Xingfa, G., Qingxi, T., Lanfen, Z., Bing, Z., 2002. Relating soil surface moisture to reflectance. Remote Sens. Environ. 81, 238–246. http://dx.doi.org/10.1016/S0034-4257(01)00347-9.

Wiesmeier, M., Barthold, F., Blank, B., Kögel-Knabner, I., 2011. Digital mapping of soil organic matter stocks using Random Forest modeling in a semi-arid steppe ecosystem. Plant Soil 340, 7–24. http://dx.doi.org/10.1007/s11104-010-0425-z.

Williams, P., Norris, K., 1987. Near-infrared technology in the agricultural and food industries, 330 pp.

Xiong, X., Grunwald, S., Myers, D.B., Kim, J., Harris, W.G., Comerford, N.B., 2014. Holistic environmental soil-landscape modeling of soil organic carbon. Environ. Modell. Softw. 57, 202–215. http://dx.doi.org/10.1016/j.envsoft.2014.03.004.

Zhang, H.K., Huang, B., 2015. A new look at image fusion methods from a Bayesian perspective. Remote Sens. 7, 6828–6861. http://dx.doi.org/10.3390/rs70606828.

Zhang, J., 2010. Multi-source remote sensing data fusion: status and trends. Int. J. Image Data Fusion 1, 5–24. http://dx.doi.org/10.1080/19479830903561035.